

Synthesis and characterization of Nickel Cobalt Sulfide (NiCo_2S_4) for supercapacitor electrodes

M.Sc. Thesis

by

Girish R. Wakale

Roll No: 210315100



to

**DEPARTMENT OF PHYSICS
INDIAN INSTITUTE OF TECHNOLOGY
INDORE**

June 2023

Synthesis and characterization of Nickel Cobalt Sulfide (NiCo_2S_4) for supercapacitor electrodes

A THESIS

*Submitted in partial fulfillment of the
requirements for the award of the degrees*

of

MASTER OF SCIENCE

by

Girish R. Wakale

Roll No: 210315100



**DEPARTMENT OF PHYSICS
INDIAN INSTITUTE OF TECHNOLOGY
INDORE**

June 2023



INDIAN INSTITUTE OF TECHNOLOGY INDORE

CANDIDATE'S DECLARATION

I hereby certify that the work which is being presented in the thesis entitled “Synthesis and characterization of Nickel-Cobalt Sulfide for supercapacitor electrodes” in the partial fulfillment of the requirements for the award of the degree of **MASTER OF SCIENCE** and submitted in the **DEPARTMENT OF PHYSICS, Indian Institute of Technology Indore**, is an authentic record of my own work carried out during the time period from August 2021 of joining the M.Sc. program to June 2023. This work is completed under the supervision of **Dr. Preeti A. Bhohe, Professor, Physics Department**, and **Dr. Rupesh S Devan, Associate Professor, MEMS Department, IIT Indore**.

The matter presented in this thesis has not been submitted by me for the award of any other degree of this or any other institute.

(Girish R. Wakale)

CERTIFICATE

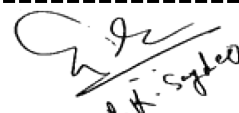
It is certified that the above statement made by the student is correct to the best of our knowledge. **Girish R. Wakale** has successfully given his M.Sc. Oral examination held on the Date: **06/06/2023**.

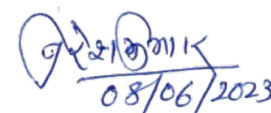
Thesis Supervisors

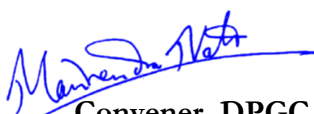

08-06-2023
Dr. Preeti Bhohe
(Department of Physics)


08-06-2023
Dr. Rupesh S. Devan
(Department of MEMS)

PSPC Members


09.06.2023
Dr. Pankaj R. Sagdeo
(Department of Physics)


08/06/2023
Dr. Naresh Kumar Kumawat
(Department of Physics)


Convener, DPGC

9/6/23

(Department of Physics)

PREFACE

The work for this report on “Synthesis and characterization of Nickel Cobalt Sulfide (NiCo_2S_4) for supercapacitor electrodes" is performed in the Nano-architectures research group of Dr. Rupesh at the Department of Metallurgical Engineering and Materials Science (MEMS), IIT Indore.

In this work, we have synthesized NiCo_2S_4 with different morphologies like nanoparticles, mesoporous hierarchical discs considering nanosheets, and microflowers consisting of nanoflakes, via hydrothermal method under optimized reaction precursors concentration, temperature, and time, etc. The structural, morphological, chemical, and electronic properties were studied by XRD, FESEM, EDS, TGA, BET, XPS, etc. The electrochemical measurements were performed by using CV, GCD, and EIS.

Girish R. Wakale
Department of Physics
IIT Indore

ACKNOWLEDGEMENT

I would like to express my special thanks of gratitude to Prof. Preeti A. Bhobe for giving me an opportunity to be part of her team. Also, I am thankful to Dr. Rupesh S. Devan for giving me the opportunity to work with him and for giving me complete access to his lab. I thank him for the constant and unmatched support which enabled this project to be carried out in such unprecedented times. His overseeing the project meant that I learned a lot while working on it. I thank him for his time and efforts. Heartfelt thank you to both of you.

I would also like to thank my lab-mates from Nano-architectures Research Group, IIT Indore, for their continuous support, company, and motivation all the time. I am grateful to Ms. Manopriya and Ms. Ekta for their guidance and assistance throughout the project. A special thanks to Mr. Santosh, Dr. Harshada, Dr. Vishesh, Ms. Sameena, Ms. Aayushi, Mr. Ajay, and Ms. Suman for the group discussion and company I had during my entire project work. The friendly environment they fostered in the lab meant a lot to me and my whole research aspect.

I would also like to express my heartfelt gratitude to the Physics Department and the Department of Metallurgical Engineering and Materials Science for providing the facilities for this research.

I will fail in my duties if I miss here to acknowledge my family. I am thankful to my whole family for providing support by all means to my life.

Girish R. Wakale.

Department of Physics

IIT Indore

ABSTRACT

In this study, we have synthesized the Nickel Cobalt Sulfide (NiCo_2S_4) using the hydrothermal method. We have optimized synthesis parameters such as reaction precursor concentration, temperature, and time to gain various morphologies, including nanoparticles, nanoplates, and nanoflakes. The morphology of the synthesized NiCo_2S_4 (NCS) sample is confirmed by Field emission scanning electron microscopy (FESEM). The X-ray diffraction spectra confirm that the obtained morphologies are of cubic crystal structure with better crystallinity without any impurity. Furthermore, the chemical and electronic properties of NCS samples were performed from Energy Dispersive X-ray Spectroscopy (EDS) and X-ray Photoelectron Spectroscopy (XPS). After that, NCS samples were drop cast over the Ni foam (1×1.5 cm in size) and used for electrochemical measurements. Cyclic voltammetry (CV) showed that the NCS samples behave like a battery-type electrode. Galvanostatic charge-discharge (GCD) studies revealed that the NCS supercapacitor electrode consisting of nanoflakes arranged in mesoporous microflowers format gained a favorable power density of 2750 W/kg at an energy density of 14.254 Wh/kg, and excellent specific capacitance of 1968.870 F/g at 2 A/g. We also performed the cyclic stability at the current density of 10 A/g, and 88.86% capacitance retained was observed after continuous 5000 charge-discharge cycles. Therefore, NCS nanoflakes are promising electrode materials to fabricate hybrid supercapacitor devices.

Table of Contents

LIST OF FIGURES.....	(15)
LIST OF TABLES.....	(17)
NOMENCLATURE.....	(19)
ACRONYMS.....	(20)
Chapter 1: Introduction	
1.1 Background.....	(21)
1.2 Chalcogenide (Sulfur) for supercapacitors.....	(23)
1.3 Nickel Cobalt Sulfide (NiCo₂S₄).....	(24)
1.4 Literature Review.....	(24)
1.5 Research gaps.....	(25)
1.6 Research objectives.....	(25)
Chapter 2: Experiment Section	
2.1 Synthesis of NiCo₂S₄.....	(27)
2.2 Methodology.....	(28)
2.2.1: X-ray diffraction (XRD).....	(29)
2.2.2: Field emission scanning electron microscopy (FESEM).....	(30)
2.2.3: Energy X-ray dispersive spectroscopy (EDS).....	(30)
2.2.4: Brunauer–Emmett–Teller (BET).....	(31)
2.2.5 Thermal gravimetric analysis (TGA).....	(32)
2.2.6 X-ray Photoelectron Spectroscopy (XPS).....	(33)
2.2.7: Electrochemical measurements.....	(34)
Chapter 3: Results and Discussion	
3.1 X-ray diffraction (XRD) Analysis.....	(39)
3.2 Field emission scanning electron microscopy (FESEM) Analysis.....	(40)
3.3 Energy X-ray dispersive spectroscopy (EDS) Analysis.....	(41)
3.4 Brunauer–Emmett–Teller (BET) Analysis.....	(42)
3.5 X-ray Photoelectron Spectroscopy (XPS) Analysis.....	(44)
3.6 Thermal gravimetric analysis (TGA) Analysis.....	(46)

3.7 Electrochemical Analysis.....	(48)
3.7.1 Cyclic voltammetry.....	(48)
3.7.2 Galvanostatic charge-discharge.....	(51)
3.7.3 Electrochemical Impedance Spectroscopy (EIS)	(52)
3.7.4 Cyclic stability.....	(53)
3.7.5 Regone plot.....	(54)

Chapter 4: Conclusion and future scope

References.....	(57)
------------------------	-------------

LIST OF FIGURES

Figure 1.1 Schematic of Supercapacitor in charging and discharging modes.

Figure 1.2 Flow chart for the types of supercapacitors.

Figure 2.1 Schematic representation of Teflon liner and the mini-stainless steel autoclave used for the NCS synthesis.

Figure 2.2 Flow chart for the synthesis procedure of NCS samples.

Figure 2.3 Image of X-ray diffraction (XRD) instrument used in the present study.

Figure 2.4 Image of the FESEM instrument used in the present study.

Figure 2.5 Image of the BET instrument used in the present study.

Figure 2.6 Types of isotherms observed in various porous materials.

Figure 2.7 Image of the equipment used for Thermogravimetric Analysis.

Figure 2.8 Schematic representation of the working principle of XPS

Figure 3.1 XRD patterns of (a) NCS4, (b) NCS6, (c) NCS8, and (d) NCS10 samples.

Figure 3.2 (a-d) Low magnification and (e-h) high magnification FESEM images of 2-D NCS for the reaction time of 4, 6, 8, and 10 hr., respectively.

Figure 3.3 EDS line spectra and Mapping of as-synthesized (a) NCS4, (b) NCS6, (c) NCS8, and (d) NCS10 samples.

Figure 3.4 (a-d) BET Surface area, (e-h) BJH pore size, and distribution of the (a) NCS4, (b) NCS6, (c) NCS8, and (d) NCS10 samples.

Figure 3.5 The reaction time-dependent variation in the surface area and pore volume distribution of the (a) NCS4, (b) NCS6, (c) NCS8, and (d) NCS10 samples.

Figure 3.6 XPS spectra of (a) S(2p), (b) Co(2p), and (c) Ni(2p) core levels of as-synthesized NCS10 sample.

Figure 3.7 (a-d) TGA curves and (e-h) DSC curves of NiCo₂S₄ sample prepared at the reaction time of (a) NCS4, (b) NCS6, (c) NCS8, and (d) NCS10 samples, respectively.

Figure 3.8 CV curves of (a) NCS4, (b) NCS6, (c) NCS8, and (d) NCS10 samples at various scan rates

Figure 3.9 The peak current density (i_p) of the cathodic peak current of different (a) NCS4, (b) NCS6, (c) NCS8, and (d) NCS10.

Figure 3.10 GCD curve of (a) NCS4, (b) NCS6, (c) NCS8, and (d) NCS10 samples recorded at various current densities in the range of 2 to 10A/g. The 2.1, 2.7, 2, and 2 mg mass was loaded to prepare the electrode of NCS4, NCS6, NCS8, and NCS10 samples, respectively.

Figure 3.11 The specific capacitance of (a) NCS4, (b) NCS6, (c) NCS8, and (d) NCS10 samples at various current densities

Figure 3.12 Electrochemical Impedance Spectra of NCS10 electrode. Inset shows the equivalent circuit diagram observed for fitted data.

Figure 3.13 Cycling stability studies of NCS10 electrode for 5000 continuous GCD cycles.

Figure 3.14 Ragone plot (specific energy and specific power) of the supercapacitor electrode NCS10 sample.

LIST OF TABLE

1.1 Table of literature review

NOMENCLATURE

i_p	Peak current
v	Scan rate
C_s	Specific capacitance
C	Specific capacity
V	Potential at working electrode vs. reference electrode
d_{hkl}	Interplanar spacing on (hkl) plane.
X	Adsorbed gas quantity.
X_m	Monolayer adsorbed quantity
P	Equilibrium pressure
P_o	Saturation pressure
C	BET constant
i	Current m Mass of active material
E	Potential window in which potential is swept.
Δt	Discharge time in GCD
R	Corrosion rate
M	Atomic weight of the metal
n	Number of electrons involved in the corrosion reaction.
F	Faraday's constant
ρ	Density of metal
R_s	Solution resistance
R_{CT}	Charge transfer resistance
C_{PE}	Constant phase element
W_Z	Warburg's impedance

ACRONYMS

FESEM	Field Emission Scanning Electron Microscope
XRD	X-ray Diffraction
XPS	X-ray Photoelectron Spectroscopy
EDS	Energy Dispersive X-ray Spectroscopy
BET	Brunauer-Emmett-Teller
BJH	Barrett-Joyner-Halenda
EIS	Electrochemical Impedance Spectroscopy
OCP	Open Circuit Potential
LSV	Linear Sweep Voltammetry
EDLC	Electric Double-Layer Capacitance
rGO	Reduced Graphene Oxide
AC	Activated Carbon
SA	Surface Area
CSA	Cross-Sectional area of Adsorbate
SCE	Saturated Calomel Electrode
NiCo ₂ S ₄	Nickel Cobalt Sulfide
NCS	NiCo ₂ S ₄
NCS/NiF	Nickel Cobalt Sulfide on Nickel foam

Chapter 1

Introduction

1.1 Background

The performance of electrochemical energy storage devices is improving continuously because of the development of vibrant advanced electrode active materials and novel device architectures [1]. These advanced electrode materials and device structures can be explored for more real-time applications. However, there are still many challenges and limitations in advanced EES systems, such as search of better electrode material, simple and cost-effective synthesis methods, reliable methodologies for electrode performance evaluation, and many more. Among the different energy storage devices, supercapacitors (SCs) are preferred one because of their many advantages over the others [1].

Supercapacitor is a device that bridges the gap between high energy density devices like batteries and traditional capacitors. They supply energy at higher power outputs than batteries and store more energy than capacitors. This device is already used in various applications, alone or in conjunction with other electrochemical energy storage technologies (mostly batteries). The basic working principle of the electrochemical capacitor is as follows: it comprises two electrodes, i.e., positive and negative, an aqueous electrolyte, and a separator which enables easy transfer of ions and prevents the device from short circuit.

As shown in Fig. 1, SCs are well-known energy storage devices providing higher capacitance (100–1000 F) than conventional capacitors, high power density, longer lifetime, high efficiency, good cyclic stability, low internal resistance, ease of fabrication, low cost and environmentally benign, etc. [1] The selection of novel electrode active material is an important aspect for the development of high-performance supercapacitors for better electrochemical performance [2]. The electrode material should possess the properties such as non-toxicity, environmentally friendly, large specific surface area, controllable porosity, desirable electroactive sites, and high and stable electrical and thermal conductivity.[2] In addition, electrolytes should be equally important to increase the device performance. Their intriguing features

should be the inertness of electrolytes with an electrode material, low toxicity, inflammability, a broad operating temperature range, wide potential window, and matching of ion size with pore size to fully utilize the surface of the porous electrode materials. [3]

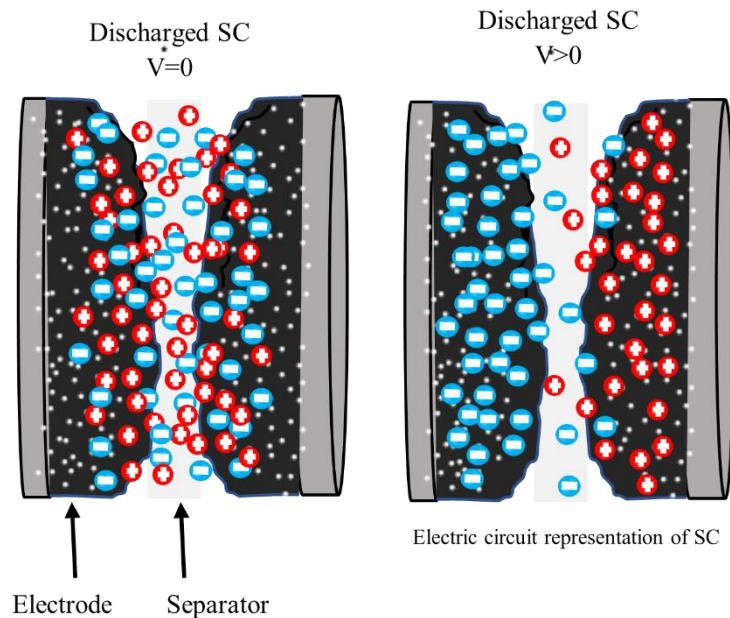


Fig. 1.1. Schematic of Supercapacitor in charging and discharging modes.

Supercapacitors are classified into three types based on their charge storage mechanisms, as shown in Fig. 1.1. namely, Electric double-layer capacitors (EDLCs), pseudocapacitors, and hybrid supercapacitors. EDLCs exclusively store charge electrostatically in the Helmholtz layer over carbon-based electrode material with very high specific surface area. Pseudocapacitors store charge electrochemically in a faradaic manner, causing some charge transfer across the contact, where mainly transition metal oxides or chalcogenides are used. [4] Fast surface redox processes and a double-layer method are used here to store charge. The hybrid capacitors combine the pseudocapacitive and EDLC electrodes [5]. These can either be of the asymmetrical or symmetrical variety, where one electrode is entire of the EDLC type while the other is entire of the pseudocapacitive type, or these various materials can be combined to create a composite that is then used as a supercapacitor.

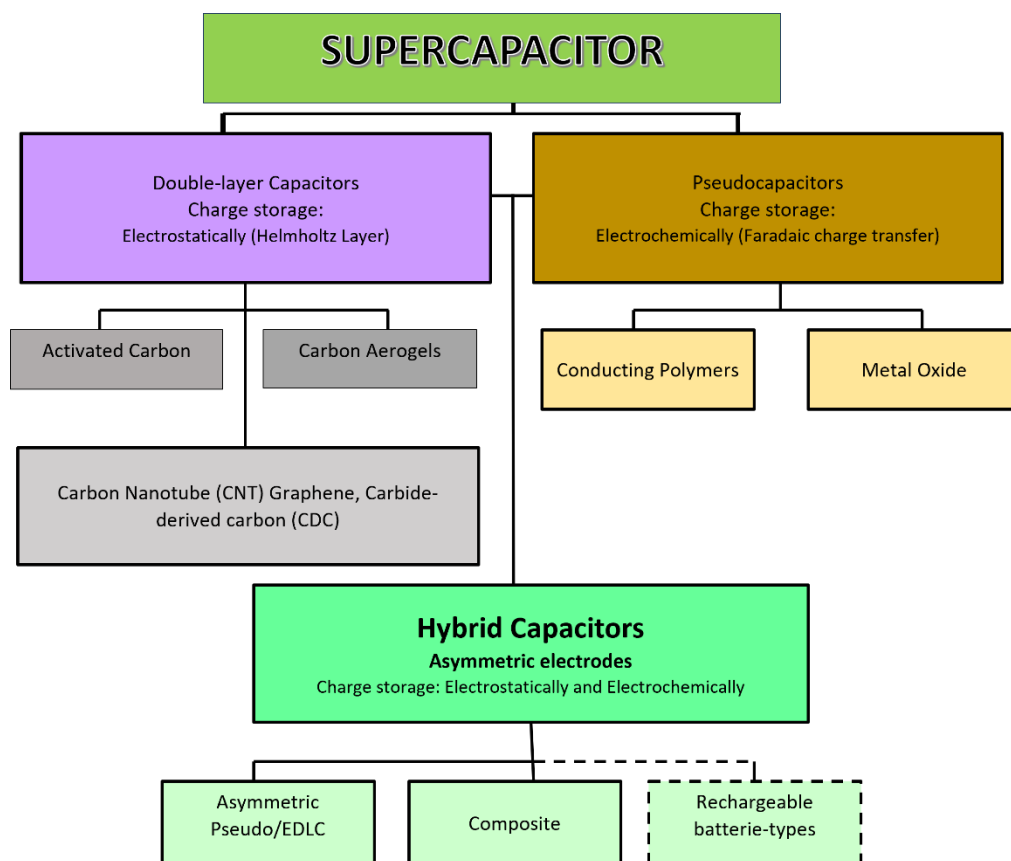


Fig. 1.2. Flow chart for the types of supercapacitors

1.2 Chalcogenides (Sulfur) for supercapacitors:

Chalcogenides are intriguing electrode materials for Li-ion batteries and supercapacitors. The redox mechanism of metal sulfides is enhanced by the regulated stoichiometry of metal and sulfur, tunable/changeable metal valences, and nanostructure morphologies.[6] Additionally, wide bandgap metal sulfides achieve electrical conductivity superior to oxides. Therefore, different metal sulfides used as electrodes in pseudo-supercapacitors, such as CuS , NiS_x , CoS_x , FeS_x , CuSbS_2 , $\text{M-Co}_2\text{S}_4$, CoNi_2S_4 , and NiCo_2S_4 , have provided better capacitance, energy/power density, and stability than their corresponding oxides.[7] Several one-dimensional (1D), two-dimensional (2D), and hierarchical morphologies have been investigated for energy storage electrodes. These morphologies provide a greater surface area for ion transport and redox kinetics. [8] On the other hand, the mesoporous architecture of metal sulfides in three dimensions (3D) hierarchical morphologies offers a higher surface-to-volume ratio for better ion transport and, consequently, greater electrochemical energy storage.[9] However, until recently, it was not easy to achieve the

hierarchical growth of 2D nanostructures, providing remarkable interconnecting paths for flawless and quicker ion transport in the supercapacitor electrode.

1.3 Nickel Cobalt Sulfide (NiCo₂S₄):

Due to strong redox activity, favorable capacitive properties, and generally good cyclic stability, NiCo₂S₄, one of the most capable and promising metal chalcogenides, has earned interest. The significant properties of binary metal sulfide are better electrical conductivity and larger theoretical specific capacity than those of a metal sulfide, have also drawn considerable attention.[10] Therefore, to enhance the electrochemical performance of materials, particularly 3D hierarchical NCS materials, researchers combine the inherent benefits of a multidimensional structure and the distinct superiority of a binary metal sulfide.

1.4 Literature Reviews

Electrode Material	Electrolyte	Cs (F/g) @ Current Density (A/g)	E _a (Wh/kg) & P _a (W/kg)	Cyclic Stability	Ref.
NiCo ₂ S ₄ /hierarchical porous carbon	6 M KOH	1863 @ 1	19, 3.9	73.1% @ 5000 cycles	[11]
NiCo ₂ S ₄ Nanoflowers @ NiCo ₂ S ₄ nanosheets	3 M KOH	1862 @ 4	18.04, 750	89% @ 4000 cycles	[12]
NiCo ₂ S ₄ nanospheres/reduced graphene oxide	6 M KOH	1406 F/g @ 1	51.7, 762	82.36% @ 2000 cycles	[13]
Bimetallic sulfide NiCo ₂ S ₄ nanowire	1 M KOH	527.8 @ 0.2	93.43, 700.7	81.8% @ 5000 cycles	[14]
NiCo ₂ S ₄ nanosheets	3 M KOH	1956 @ 1	18.75, 6030	91.6% @ 5000 cycles	[15]
NiCo ₂ S ₄ nanosheets	2 M KOH	505.6 @ 0.5	11.7, 2400	99% @ 5000 cycles	[16]
NiCo ₂ S ₄ /Ni-Co layered double hydroxide	3 M KOH	1765 @ 1	57.8, 1600	56% @ 2000 cycles	[17]
NiCo ₂ S ₄ embedded in carbon fiber	6 M KOH	1169 @ 1	28.8, 878.3	87.2% @ 10000 cycles	[18]
Spinous NiCo ₂ S ₄ nanotubes	6 M KOH	630 @ 1	52.34, 2206.37	91% @ 3000 cycles	[19]

Polypyrrole-wrapped NiCo ₂ S ₄ nanoneedles	3 M KOH	1842.8 @ 1	41.2, 402.2	92.8% @ 5000 cycles	[20]
NiCo ₂ S ₄ nanoparticles @ N-doped CNT	6 M KOH	783.5 C/g @ 1	49.75, 774.65	88.9% @ 3000 cycles	[21]
sandwich-type NiCo ₂ S ₄ @ reduced graphene oxide	2 M KOH	2003 @ 1	21.9, 417.1	86% @ 3500 cycles	[22]
NiCo ₂ S ₄ nanostructured arrays on carbon fiber paper	2 M KOH	1154 @ 1	17.3, 3200	76.7 % @ 8000 cycles	[23]
NiCo ₂ S ₄ /NiS Hollow Nanospheres	3 M KOH	1947.5 @ 3mA/cm ²	43.7, 160	90.3% @ 1000 cycles	[24]

Table 1.1 Table of literature review

1.5 Research gaps:

- Limited work has been focused on the effect of morphology variation of NiCo₂S₄ based electrode materials and their device performance.
- The way to boost the electrochemical properties of this nanomaterial as compared to the existing reports has not been thoroughly explored.

1.6 Research objectives:

- To synthesize a variety of nanostructure morphologies of NiCo₂S₄ at optimized reaction conditions.
- To analyze the structural, chemical, elemental, morphological, and electrical properties of NiCo₂S₄ nanostructures.
- To investigate the electrochemical properties of NiCo₂S₄ nanostructures using CV, GCD, and EIS.
- To improve device performance, such as high-power density and energy density with good cyclic stability, we deliberately plan to synthesize NiCo₂S₄ nanostructure with optimized parameters.

Chapter 2

Experimental Section

2.1 Synthesis of NiCo₂S₄:

Nickel nitrate hexahydrate (Ni(NO₃)₂·6H₂O), Cobalt nitrate hexahydrate (Co(NO₃)₂·6H₂O), and Thiourea (NH₄CSNH₄; 99% pure) of analytical grade was mixed in a stoichiometric ratio (1:2:4)M in 40 ml DI Water followed by stirring. Methylamine (100 μl) was added dropwise to the above solution and further kept for stirring. Furthermore, the solution was reacted in the stainless-steel autoclave oven (Fig. 2.1) at 140°C for 4h. The above process was repeated for 6h, 8h, and 10h duration for reaction. The prepared NiCo₂S₄ samples were identified as NCS4, NCS6, NCS8, and NCS10 for 4h, 6h, 8h, and 10h reaction times, respectively. The flow chart in Fig. 2.2 presents the whole synthesis process.

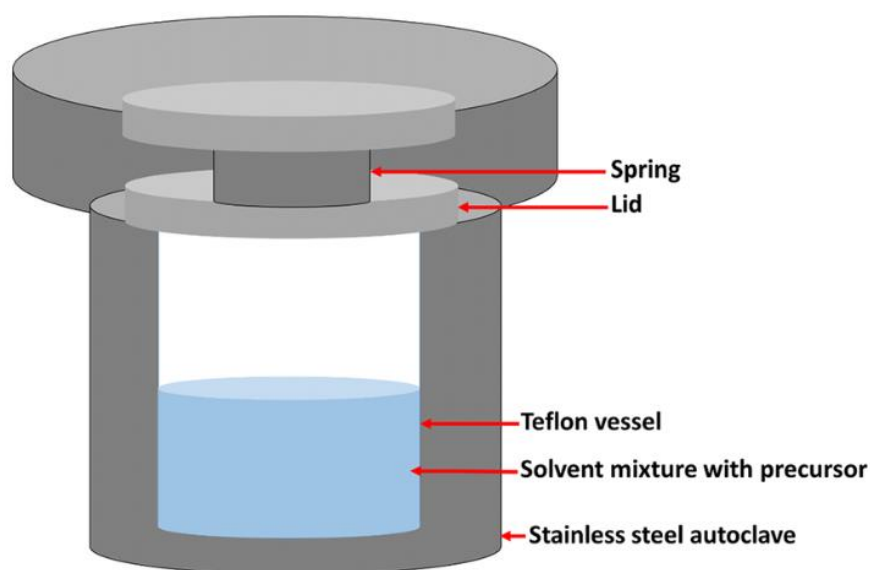


Fig. 2.1. Schematic representation of hydrothermal setup used for the NCS synthesis [25].

Synthesis of NiCo₂S₄ Nanostructures

1M (Ni(NO₃)₂·6H₂O), 2M (Co(NO₃)₂·6H₂O) and 4M of thiourea (NH₄CSNH₄) was mixed in a 40 ml DI water followed by stirring.

Methylamine (100 μl) was added to the above solution and further kept for stirring.

The solution was transferred to a stainless-steel autoclave and kept in an oven.

140° C –
4h
(NCS 4)

140° C –
6h
(NCS 6)

140° C –
8h
(NCS 8)

140° C –
10h
(NCS 10)

The solution was centrifuged with DI water and ethanol and the obtained powder was NiCo₂S₄ sample.

Fig. 2.2. Flow chart for the synthesis procedure of NCS samples.

2.2. Methodology

The surface morphology of NiCo₂S₄ nanostructures were examined using FESEM (JEOL, JSM-7610 F Plus), and EDS (Oxford, X-MAX), respectively. The crystal structure and lattice parameters were analyzed from an XRD (Empyrean-DY2528, Malvern Panalytical, $\lambda_{\text{Cu}} = 1.5405 \text{ \AA}$). Chemical states and electronic structure were investigated from XPS endowed with monochromatic Al-K α X-rays (Thermo Scientific Inc.). The pore size distribution and surface area were determined Barrett-Joyner-Halenda (BJH) and Brunauer Emmett Teller (BET) methods carried out in a gas sorption

analyzer (Quantchrome Autosorb iQ2), and the electrochemical measurements were done by an electrochemical workstation (Autolab, PGSTAT302N, Metrohm) to study the redox kinetics of NiCo₂S₄ samples.

2.2.1. X-ray diffraction (XRD)

An efficient and popular tool for characterizing materials is powder X-ray diffraction (XRD). In addition to numerous microscopic and spectroscopic techniques, phase identification, crystallite size, and sample purity are some of the crucial details that powder XRD analysis of a sample can provide. Because it is a bulk method, the data it produces can be compared to microscopic data to determine whether microscopic findings on a small sample of particles are typical of the entire sample. Other essential details of this technique are vastly reported in the literature, [26] hence avoided in this thesis. The PANalytical Empyrean X-ray diffractometer (Fig. 2.3) was used for structural analysis of the NCS samples.



Fig. 2.3. Image of X-ray diffraction (XRD) instrument used in the present study.

2.2.2: Field emission scanning electron microscopy (FESEM)

The energy storage performance of nanomaterials is always correlated with surface morphological features. Therefore, exploration of the morphologies and microstructures of the materials is one of the prerequisites. In the present case, we have used FESEM, JEOL, JSM-7610 F Plus for the morphological analysis (Fig. 2.4). Other essential details of this technique are vastly reported in the literature [27, 28] and hence avoided in this thesis.



Fig. 2.4. Image of the FESEM instrument used in the present study.

2.2.3: Energy-dispersive X-ray Spectroscopy (EDS)

Energy-dispersive X-ray spectroscopy is a powerful tool that enables the user to study the presence of elements in the required sample. The principle of EDS is to bombard high-energy beam of X-rays to remove 'core' electrons from an atom which leaves behind a hole followed by filling

up by higher – energy electron (Auger Relaxation), which releases energy. This process enables us to know the type and at what proportion of elements are present in the periodic table [29]. In the present case, we have used Oxford EDS X-MAX 20 mm. equipped with the FESEM for the elemental analysis.

2.2.4: Brunauer–Emmett–Teller (BET)

The Surface area and pore size distribution of all the NCS4 samples were analyzed using liquid N₂ to obtain the amounts of adsorption-desorption isotherm Brunauer–Emmett–Teller (BET) and Barrett-Joyner-Halenda (BJH) in an automated of nitrogen gas sorption isotherms (Autosorb IQ2 - Quantachrome Instruments) (Fig. 2.5). Other essential details of this technique are vastly reported in the literature, [30] hence avoided in this thesis. However, the five different adsorption isotherm types shown in Fig. 2.6 are essential to explain the absorption-desorption correlation.



Fig. 2.5. Image of the BET instrument used in the present study.

Type I isotherm shows monolayer adsorption; it is a pseudo-Langmuir isotherm. A Type – 1 isotherm (connected to the first monolayer's adsorption energy and varies from solid to solid) is produced when $P/P_0 = 1$ and $c > 1$ in the BET equation, where P/P_0 represents partial pressure value, and c is the BET constant and usually, this is applicable for those with pores $< 2\text{nm}$. Compared to the Langmuir model, a type II isotherm is substantially different. A monolayer was formed in the middle, with a flatter area. A type II isotherm is produced when $c > 1$ in the BET equation. When employing the BET approach, this is the most frequently obtained isotherm. At the knee, monolayer formation starts, and at medium pressure, multilayer formation happens. Capillary condensation happens at greater pressures. When the $< c1$, a type III isotherm that depicts the creation of a multilayer is achieved. Due to the curve's lack of an asymptote, neither med nor BET applies, and no monolayer is required. When capillary condensation takes place, type IV isotherms appear used for characterization of mesoporous materials with pore sizes between 2 and 50 nm. At pressures below the gas saturation pressure, gases condense in the solid's small capillary pores. It demonstrates the production of a monolayer at lower pressures, followed by the formation of multilayers. Type V isotherms are irrelevant to BET but are extremely comparable to type IV isotherms.[31]

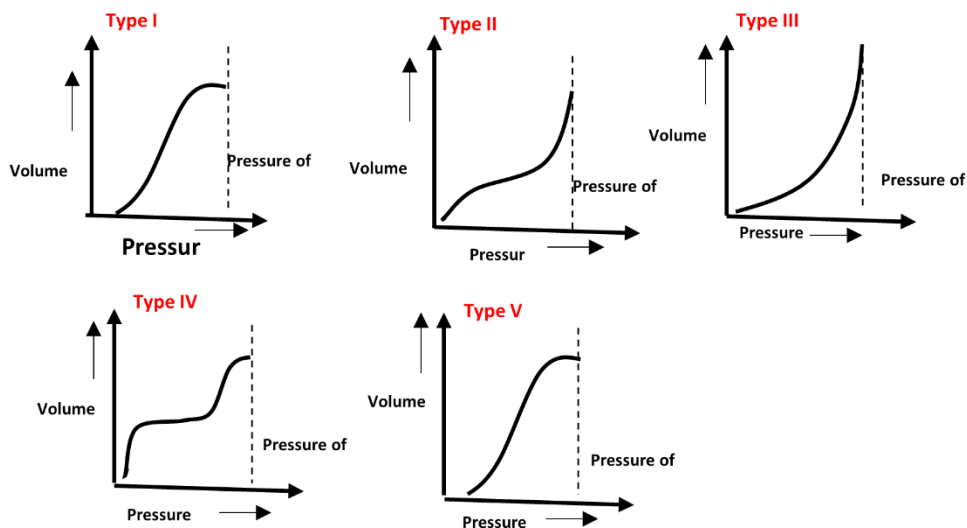


Fig. 2.6. Types of isotherms observed in various porous materials.

2.2.5 Thermal gravimetric analysis (TGA)

Thermogravimetric Analysis (TGA, (Merrler Toledo TGA/DSC system 1 stare system) is a method for characterizing materials used in various petrochemical, food, pharmaceutical, and environmental applications (Fig. 2.7). TGA assesses the composition, purity, processes leading to breakdown, temperature leading to decomposition, and absorbed moisture content of your products. Other essential details of this technique are vastly reported in the literature [32, 33] and hence avoided in this thesis.



Fig. 2.7. Image of the equipment used for Thermogravimetric Analysis [32]

2.2.6 X-ray Photoelectron Spectroscopy (XPS)

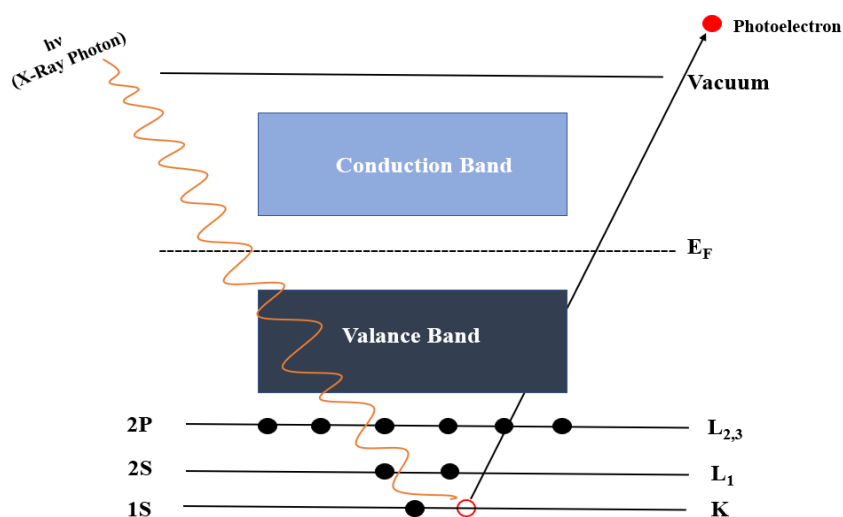


Fig. 2.8. Schematic representation of the working principle of XPS

By using XPS, a sample's surface chemistry can be ascertained. An X-ray beam is incident on the solid sample surface to obtain the XPS spectra. The electrons are ejected off the sample's top surface (1–10 nm) by these X-rays because they have sufficient energy. A record is made of the quantity and kinetic energy of the expelled electrons (Fig. 2.8). This spectrum can be used to identify the sample's elemental makeup because electrons in various shells and subshells (s, p, d, etc.) have various energies. In order to measure XPS, monochromatic Al $K\alpha$ X-rays were used on a Thermo Scientific XPS.[34]

2.2.7: Electrochemical measurements

Various electrochemical testing techniques were used to examine the prepared sample's supercapacitor behavior of the electrode material. Voltammograms or Cyclic voltammetry is an electrochemical technique used to study the redox properties of chemical species. It involves measuring the current response as a function of applied potential in a cyclic manner. The technique provides information about the electron transfer kinetics, thermodynamics, and concentration of electroactive species in a solution. The general principles of cyclic voltammetry can be described using the following steps:

Electrochemical Cell Setup: A typical electrochemical setup consists of three electrodes such as a working electrode, a reference electrode, and a counter electrode. The redox reactions occur in the working electrode, the reference electrode provides a stable reference potential, and the counter electrode completes the electrical circuit. The electrodes are emerged in an electrolyte solution containing electrolyte solution.

Potential Scan: The potential is swept linearly with time between two defined limits, typically referred to as the upper (E_{upper}) and lower (E_{lower}) potential limits. The potential scan rate (v) determines the speed at which the potential changes and is usually expressed in volts per second (V/s).

Current Measurement: The current flowing through the cell is measured as a function of the applied potential. During the forward scan (from E_{lower} to E_{upper}), the current increases or decreases depending on the flow of the redox reaction. In the reverse scan (from E_{upper} to E_{lower}), the current changes in the

opposite direction. The resulting current-potential curve is known as a cyclic voltammogram.

Analysis of Cyclic Voltammogram: The cyclic voltammogram provides information about the redox processes occurring in the solution. Key features include peak potentials (E_p), peak currents (i_p), and peak shapes. The peak potentials can be used to determine the potential (E°) of the redox couple, while the peak currents are ascribed to the concentration of the electrolyte solution and the rate of electron transfer.

The following formula represents the relationship between current (i) and potential (E) in cyclic voltammetry:

$$i = nFAc\left(\frac{v}{d}\right)^{\frac{1}{2}} \quad (1)$$

where:

i = current (A)

F = Faraday constant (C/mol)

A = electrode area (cm²)

n = number of electrons transferred in the redox reaction

c = concentration of the analyte (mol/cm³)

d = diffusion coefficient of the analyte (cm²/s)

v = scan rate (mV/s)

This equation, known as the Randles - Sevcik equation (eq 1), describes the current response in cyclic voltammetry based on the principles of mass transport and electron transfer kinetics.

Galvanic charge and discharge refer to the process of transferring electric charge into and out of a galvanic cell or battery. An external power source, such as a battery charger, is connected to the galvanic cell during the charging process. The charger applies a higher voltage than the cell's open-circuit voltage, which causes a drift of electric current into the electrochemical cell. The cell undergoes an oxidation reaction at the anode, where electrons are released, and a reduction reaction occurs at the cathode, where electrons are gained. This charging process results in the restoration of the reactants within the cell. Conversely, during the discharge process, the galvanic cell is connected to an external circuit, and the chemical reactions within the cell generate an electric current. The reactants inside

the cell are consumed, undergoing oxidation at the anode and reduction at the cathode, which produces electrical energy that can be used to power devices or perform work.

The galvanostatic charge-discharge principle of a supercapacitor is like that of a regular battery or electrochemical cell. It involves applying a constant current to the supercapacitor during the charge and discharge processes. This allows for controlled energy transfer and monitoring the supercapacitor's performance [36]. Here is an explanation of the galvanostatic charge-discharge principle for a supercapacitor:

1. Galvanostatic Charge:

- During the galvanostatic charging process of a supercapacitor, a constant current is applied to the supercapacitor.
- The applied current forces the migration of ions from the electrolyte to the electrode surfaces, where they are adsorbed onto the porous electrode material.
- This charge storage at the electrode-electrolyte interface results in an increase in the supercapacitor's stored electrical energy.

2. Galvanostatic Discharge:

- In the galvanostatic discharge process, the supercapacitor is connected to a load or external circuit, and a constant current is drawn from the supercapacitor.
- As the current flows, the stored energy in the supercapacitor is released.
- The adsorbed ions at the electrode surfaces are desorbed back into the electrolyte, and the supercapacitor's potential gradually decreases.

The galvanostatic charge-discharge process of a supercapacitor is typically faster compared to batteries due to the electrostatic nature of energy storage. Supercapacitors can deliver high power densities, making them suitable for applications requiring rapid energy transfer and high burst power. During galvanostatic charge and discharge, it is essential to consider the voltage and current limits specified by the manufacturer to avoid overcharging or over-discharging the supercapacitor, which can affect its performance and longevity.

The EIS method was used to investigate how electrode material behaved in terms of resistance and capacitance. The electrochemical impedance spectrum (EIS) of a single electrode or electrochemical cell comprises both imaginary and real components. To determine the contribution of the resistance of the material in the charge storage mechanism, the frequency is varied across a predetermined range to produce the impedance spectrum.[37]

An analytical method for characterizing electrochemical cells over a range of frequency regimes is electrochemical impedance spectroscopy (EIS). Unlike CV and GCD studies, EIS studies are performed on systems to measure the impedance offered by the cell as a function of frequency (frequency ranges from 100 kHz down to 10 mHz).[38]

When representing impedance data, there are two typical methods:

- i) The phase angle (Φ) and absolute impedance modulus (Z) are shown on the Bode plot as a function of frequency and phase angle.
- ii) The Nyquist plot depicts real and imaginary impedances at various frequencies and is more frequently observed. In order to analyze diverse behaviors for the various frequency regimes, impedance measurements are often performed and plotted from the high-frequency domain to the low-frequency domain. The equivalent series resistance (ESR) of the electrochemical cell is determined by the Nyquist plot's real axis (X-axis) impedance point at the highest frequencies with respect to the real axis of impedance, subsequent semicircles, aligned at an angle of 45° line and a 90° angle represents the charge storage mechanisms of the type of capacitive materials.[35]

EIS involves applying an AC (alternating current) signal to the system over various frequencies and measuring the resulting impedance. Here are explanations of some of the technical terms associated with EIS:[38]

1. **Solution Resistance (R_s):** Solution resistance refers to the resistance of the electrolyte solution in which the electrochemical system is immersed. It represents the resistance encountered by the AC current

as it passes through the solution. Solution resistance is typically considered a constant value that can be subtracted from the measured impedance.

2. **Charge Transfer Resistance (R_{ct}):** Charge transfer resistance represents the resistance linked with the charge transfer process happening at the electrode-electrolyte interface. It is related to the kinetics of the electrochemical reactions taking place. A higher charge transfer resistance indicates slower reaction kinetics and can be an indicator of sluggish electrode processes or electrode fouling.
3. **Warburg Impedance:** Warburg impedance is a term that describes the impedance associated with diffusion processes occurring in the electrochemical system. It arises due to the transport of species (such as ions or molecules) from the bulk solution to the electrode's surface. Warburg impedance is often observed as a sloping line at lower frequencies on the EIS plot.
4. **Constant Phase Element (C_{PE}):** A constant phase element is a feature which represents an equivalent circuit element that represents the behavior of non-ideal capacitive processes. It can model systems that deviate from the ideal behavior of a pure capacitor. The CPE is characterized by a constant phase angle instead of a fixed capacitance value.
5. **Equivalent Series Resistance (ESR):** Equivalent Series Resistance refers to the overall resistance of the electrochemical system, including resistive components such as solution resistance, charge transfer resistance, and other sources of resistance within the system. ESR provides information about the total resistance encountered by the AC current.

Interpreting the EIS plot requires considering the context of the specific electrochemical system being studied and often involves fitting the experimental data to appropriate equivalent circuit models to extract quantitative information about the system's properties and processes.

Chapter 3

Results and Discussion

3.1 X-ray diffraction (XRD) Analysis

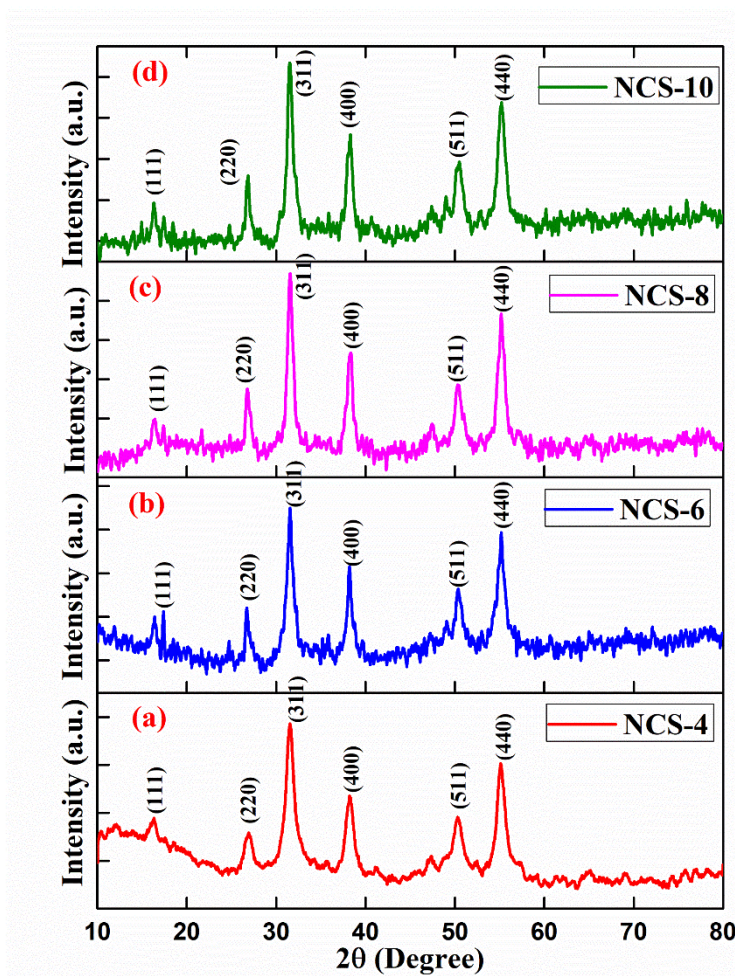
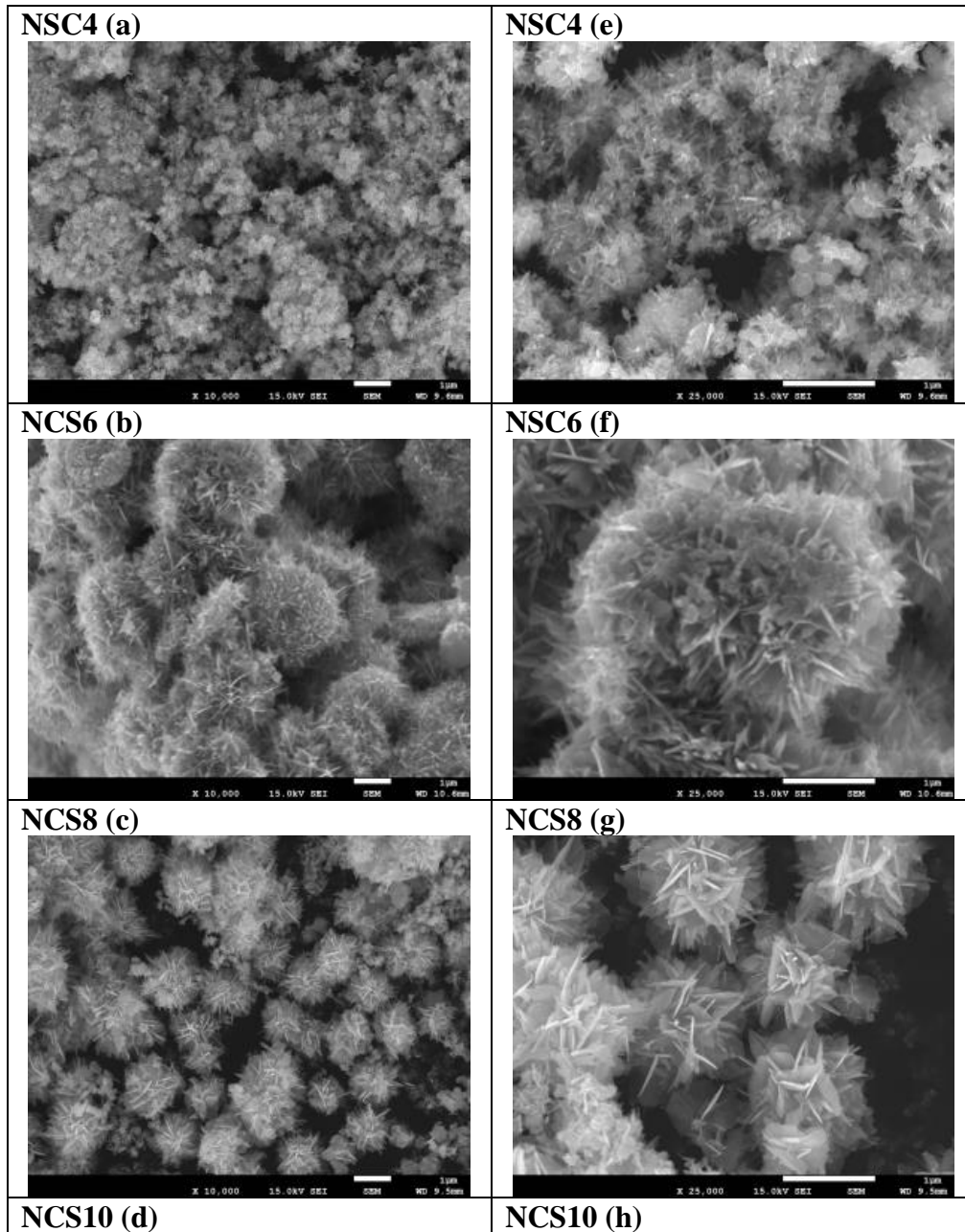


Fig. 3.1. XRD patterns of (a) NCS4, (b) NCS6, (c) NCS8, and (d) NCS10 samples.

The XRD pattern of the synthesized sample is shown in Fig. 3.1 represents the Cubic crystal structure of NiCo_2S_4 . The major diffraction peaks of the as-synthesized powder sample located at $2\theta = 31.475^\circ$, 38.193° , and 55.303° with space group Fd-3m are well indexed to the lattice planes of (311)

(400) and (440), respectively, with lattice constants of $a = 9.417 \text{ \AA}$, $b = 9.417 \text{ \AA}$ and $c = 9.417 \text{ \AA}$, and $\alpha, \beta, \gamma = 90^\circ$ which are in good agreement with the JCPDS Card No. 43-1477. The high background might be due to the effect called fluorescence.[39]

3.2 Field emission scanning electron microscopy (FESEM) Analysis.



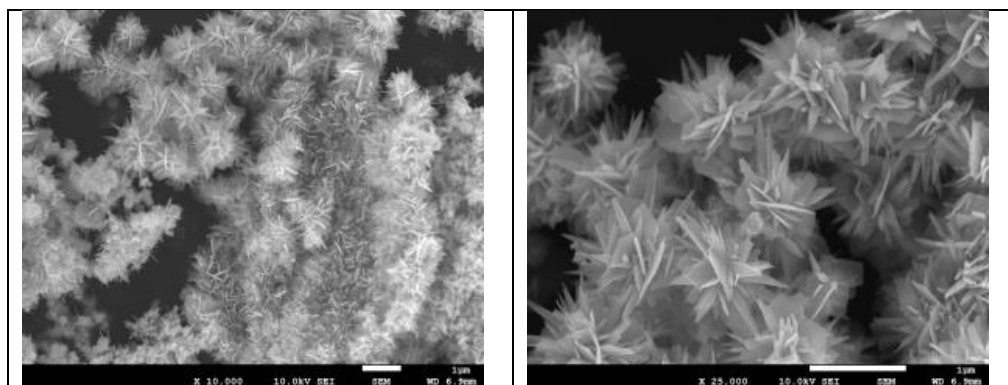


Fig. 3.2. (a-d) Low magnification and (e-h) high magnification FESEM images of NCS samples prepared at reaction times of 4, 6, 8, and 10 h., respectively.

Fig. (3.2) shows the surface morphological features of NCS samples synthesized at various reaction times. At low magnification, FESEM images (Fig.3.2 (a-d)), the uniformity of the surface morphologies were observed for all reaction times. The FESEM images (Fig.3.2(e-h)) confirmed the transformation of growth initiation of nanoparticles to well-grown microflowers with increased reaction time. At 4h, the initiation of nucleation sites for the growth of nanostructures was observed. When the reaction time was increased to 6h, it was transformed to well-grown 2D nanosheets grown in the form of hierarchical 2D discs. The 2D nanosheets were further transformed into rose-like micro flowers. After the reaction time of 8h and at 10 h, the growth of microflowers was more distinct, consisting of nanoflakes. With a longer reaction, the growth species have enough time to interact with their neighboring sites and transform into spherical rose-like microflowers of 2D nanoflakes.

3.3 Energy X-ray dispersive spectroscopy (EDS)

The EDS line spectra and mapping of all the samples are shown in Fig. 3.3. The EDS of the NCS4 and NSC6 sample confirms the presence of Nickel, Cobalt, and Sulfur. Additionally, a significant amount of oxygen is found in NCS4 and NCS6 since the sample surface oxidized due to atmospheric oxygen or the unreacted hydroxyl group. This demonstrated the morphological creation of cobalt oxysulfide nanostructures. The EDS spectra of the NCS8 and NCS10 samples confirm the presence of elements Nickel, Cobalt, and Sulfur only. Whereas a peak for oxygen was not detected, which might be due to the completion of the sulfurization reaction in 8 and 10h.

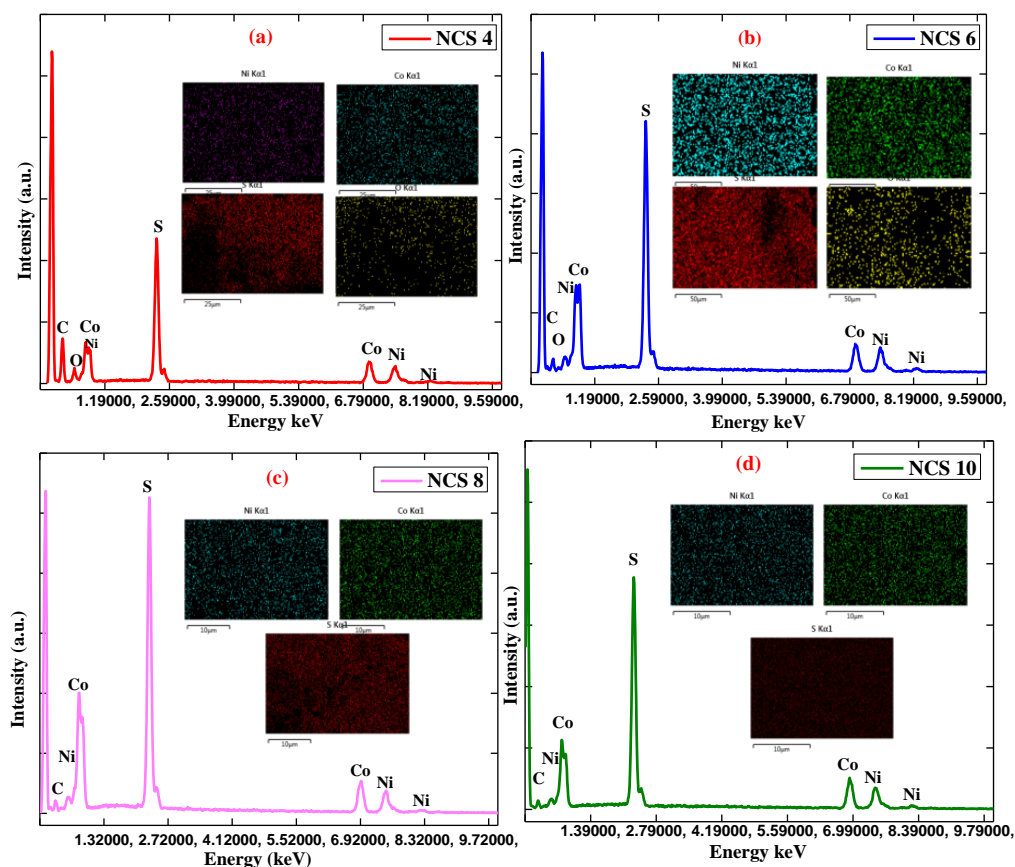


Fig. 3.3. EDS line spectra and Mapping of as-synthesized (a) NCS4, (b) NCS6, (c) NCS8, and (d) NCS10 samples.

3.4 Brunauer–Emmett–Teller (BET) Analysis

The surface properties, such as pore size/volume and specific surface area, were analyzed from N_2 adsorption and desorption measurements. The N_2 isotherm of the $NiCo_2S_4$ displays adsorption–desorption curves which correspond to the Type – III hysteresis loop in the P/P_0 region of 0.4 – 1.0, which mesoporous hierarchical 2D flakes (Fig. 3.4(a-d)). Furthermore, BJH pore diameter distribution of $NiCo_2S_4$ was observed in the range of 3 nm–350 nm (Fig. 3.4(e-h)). The BET specific surface area is found to be 36.671 m^2/g for NCS4, 37.057 m^2/g for NCS6, 33.412 m^2/g for NCS8, and 28.163 m^2/g for the NCS10, respectively, indicating a large surface area that offers ample electroactive sites and short diffusion routes for charge transport. The pore diameter was relatively narrow such as 3.831 nm for NCS4, 3.058 nm for NCS6, 3.061 nm for NCS8, 3.412 nm for NCS10 (Fig. 3.5). These characteristics are thought to be very advantageous for its use in electrochemical energy storage device.

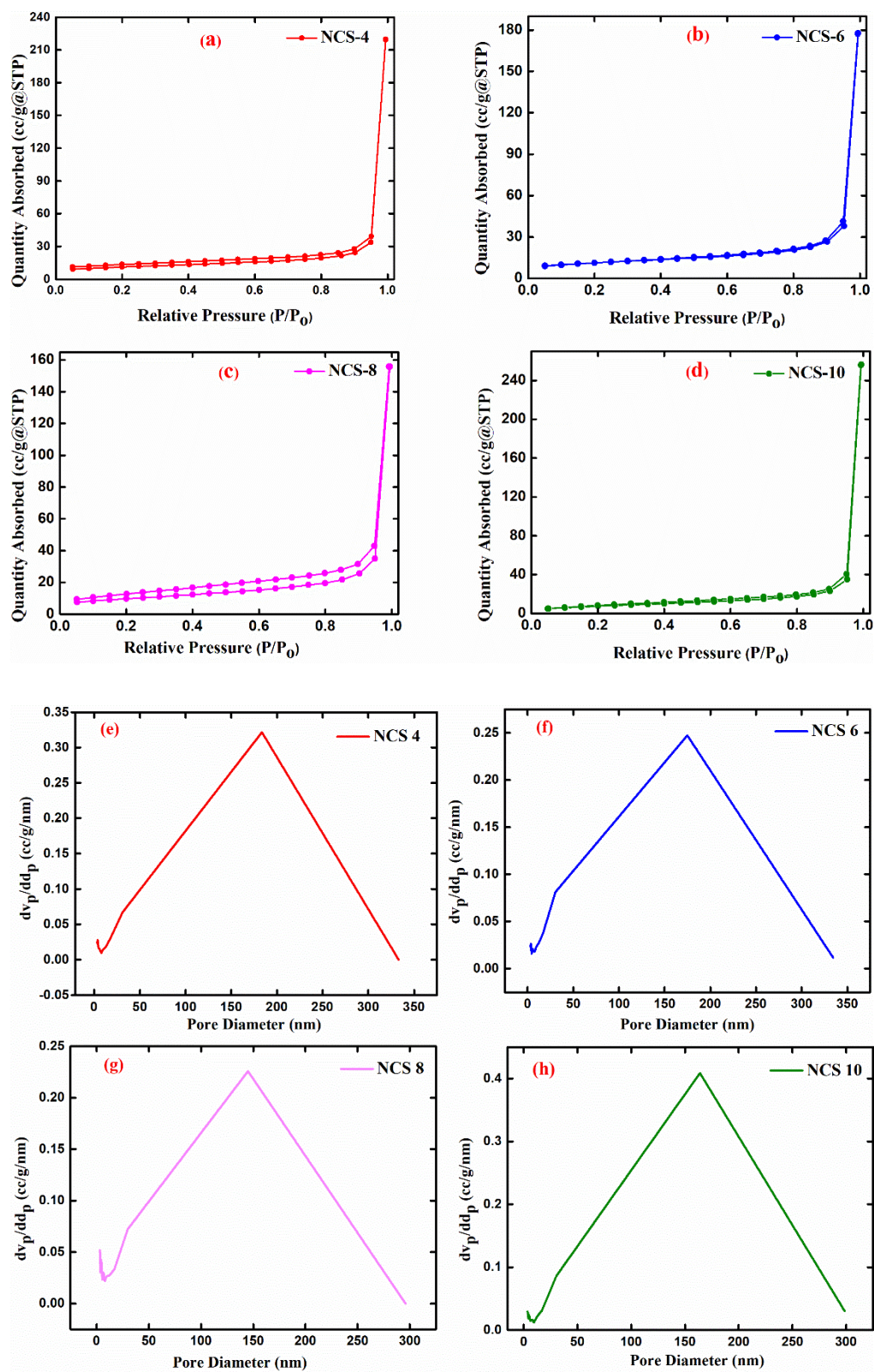


Fig. 3.4. (a-d) BET Surface area, (e-h) BJH pore size, and distribution of the (a) NCS4, (b) NCS6, (c) NCS8, and (d) NCS10 samples

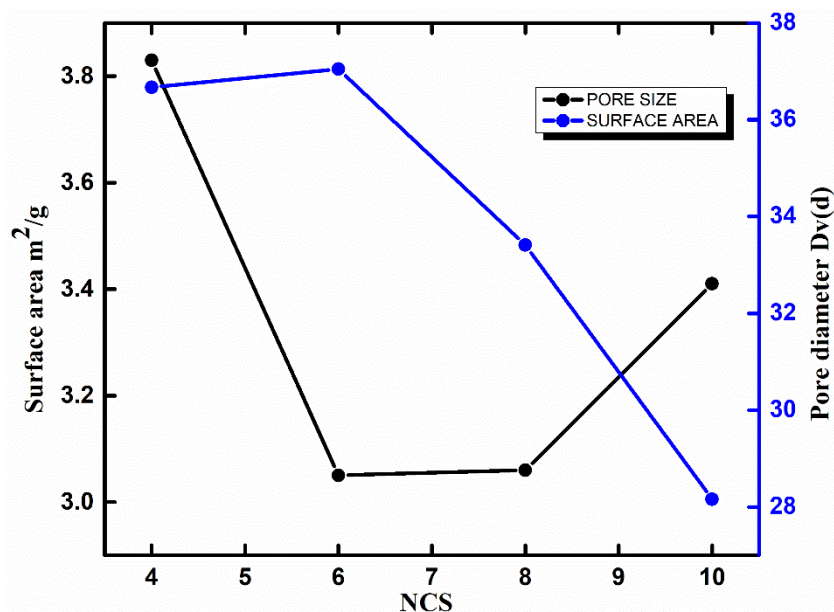


Fig. 3.5. The reaction time-dependent variation in the surface area and pore volume distribution of the (a) NCS4, (b) NCS6, (c) NCS8, and (d) NCS10 samples.

3.5 X-ray Photoelectron Spectroscopy (XPS) Analysis

Figure. 3.6 displays the high-resolution XPS spectra of the $NiCo_2S_4$. All the peaks are deconvoluted with Voigt fitting function using Shirley background. The binding energies of 778.72 (a), 781.55 (a'), 786.03 (s), 793.72 (b), and 796.71 (b'), 801.23 (s') eV explicitly fit into the deconvoluted spectrum (Fig 3.6b). The core levels of $Co^{2+}(2p_{3/2})$, $Co^{3+}(2p_{3/2})$, $Co^{2+}(2p_{1/2})$, and $Co^{3+}(2p_{1/2})$ are arbitrated by peaks a, a', b, and b', respectively [34]. However, the Co^{3+} cations are barely present, as evidenced by the higher intensity of the $Co^{2+}(2p_{3/2})$ core levels compared to those of $Co^{3+}(2p_{3/2})$. $Co^{2+}(2p)$ core levels exhibit the 15 eV spin-orbit splitting. The peak b, which has a binding energy of 781.55 eV, denotes the peak associated with the shake-up. Additionally, the S(2p) XPS spectra with compound peak features were decomposed using the Shirley background and the Voigt fitting function. For three peaks at BE of 161.54 (a), 162.69 (a'), 163.86 (b), and 169.08 (c) eV, the deconvoluted spectrum fits each peak exactly. The $S^{2-}(2p_{3/2})$ and $S^{2-}(2p_{1/2})$ core level peak features are arbitrated by peaks a and b, respectively. In $S^{2-}(2p)$ core levels, the spin-orbit splitting of 7.54 eV is seen. Unreacted Sulphur in the nanostructure is shown by the peak c with a binding energy of 169.08.[40]

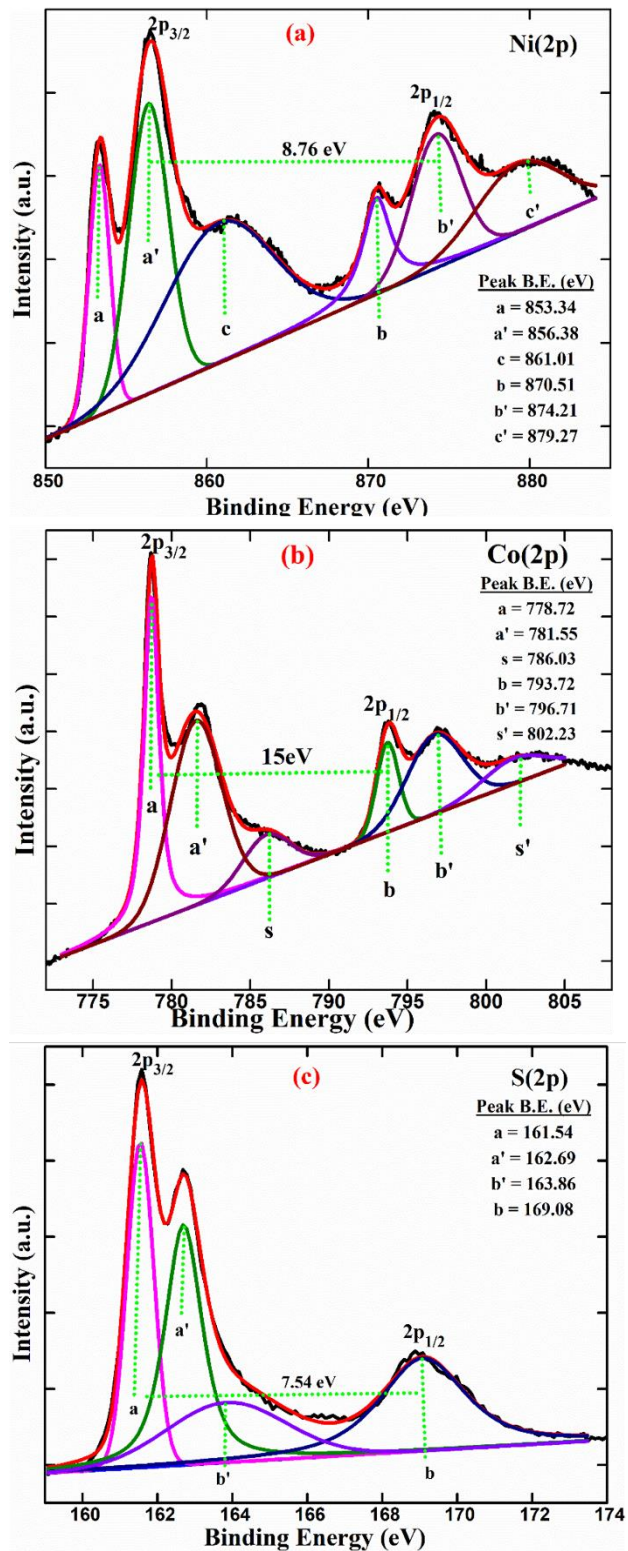


Fig. 3.6. XPS spectra of (a) Ni(2p), (b) Co(2p), and (c) S(2p), core levels of as-synthesized NCS10 sample.

The XPS spectra of Ni showed four peaks that, on deconvolution, fitted perfectly with six peaks identified as a, a', c, b, b', and c consecutively located at a binding energy of 853.34, 870.51, 856.38, 860.73, 879.27 and 874.21 eV,

which are assigned to $\text{Ni}^{2+}(2p_{3/2})$, $\text{Ni}^{3+}(2p_{3/2})$, $\text{Ni}^{2+}(2p_{3/2})$ shakeup satellite peak, $\text{Ni}^{2+}(2p_{1/2})$, $\text{Ni}^{3+}(2p_{3/2})$ and $\text{Ni}^{2+}(2p_{1/2})$ shakeup satellite peaks, respectively. NiCo_2S_4 nanosheets were formed, as demonstrated by the clearly intense peak of $\text{Ni}^{2+}(2p_{3/2})$ and $\text{Ni}^{2+}(2p_{1/2})$ core levels of Ni^{2+} ions. It is also accompanied by a Ni^{3+} peak, but their strength relative to Ni^{2+} is much lower, demonstrating their insignificance. For their satellite peaks, the $\text{Ni}^{2+}(2p_{3/2})$ and $\text{Ni}^{2+}(2p_{1/2})$ core levels' energy separation of 2.32 (± 0.2) eV remained constant.[40] Overall, the XPS analysis represents the formation of pure stoichiometric NiCo_2S_4 compounds.

3.6 Thermal gravimetric analysis (TGA) Analysis

To investigate the corresponding reactions and thermal analysis of NiCo_2S_4 nanostructures, TGA was first performed. The TGA and DSC curves of the NCS, from room temperature (RT) to 400°C in the ambient atmosphere, are shown in Fig.3.7 The weight remained constant at temperatures more than 520 °C. Additionally, it was found that the weight of NCS was almost constant between room temperature and 400 °C. When the temperature was above 400 °C, however, a notable increment in the weight of NCS was observed, which may be related to the oxidation of metal sulfides into metal sulfate and metal oxysulfide (MSO_4 and MOSO_4) [41]. The generated metal sulfate and meal oxysulfate started to break down into NiO and Co_3O_4 as the temperature reached over 700 °C till the equilibrium condition.[42]

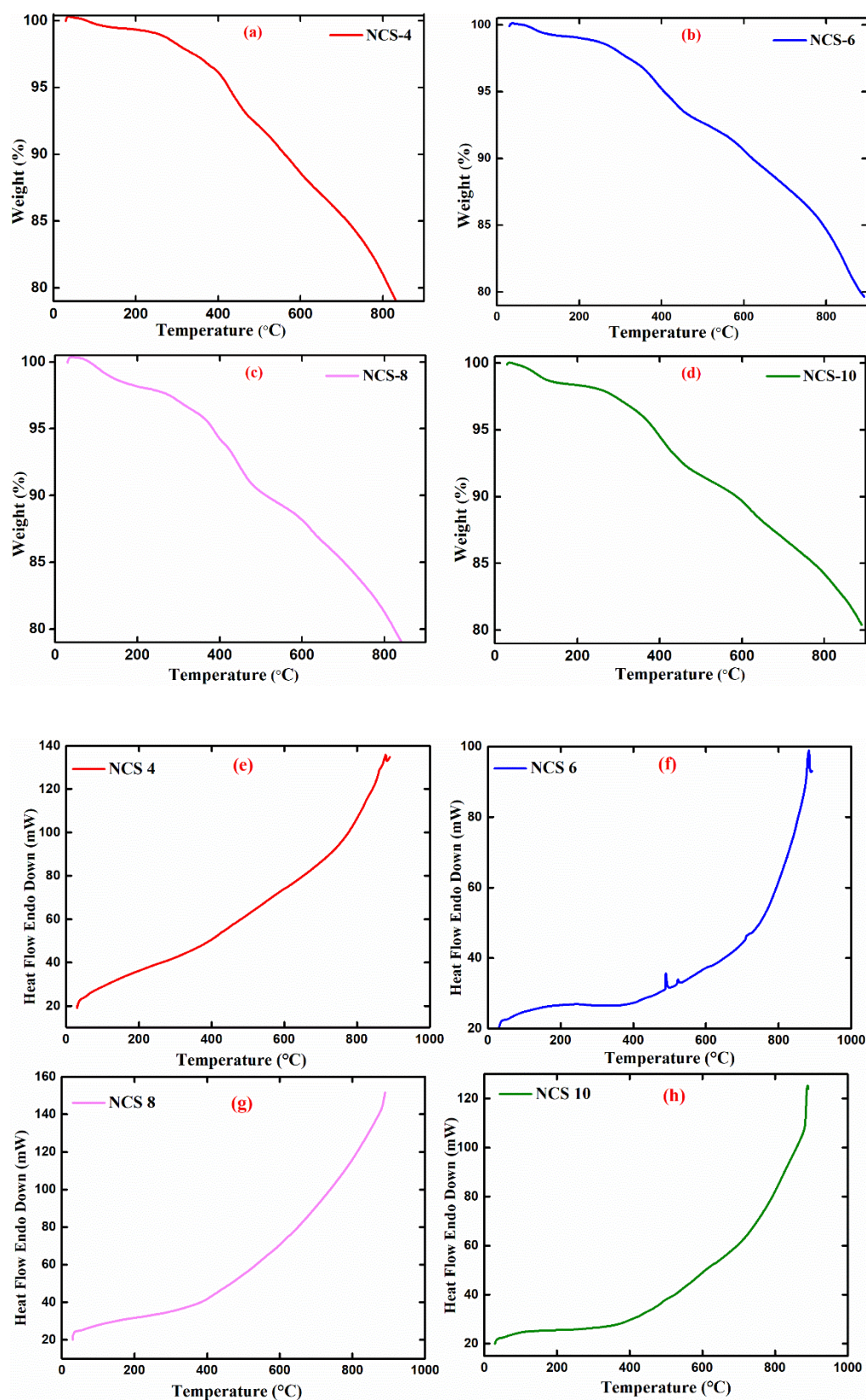


Fig. 3.7. (a-d) TGA curves and (e-h) DSC curves of NiCo₂S₄ sample prepared at the reaction time of (a) NCS4, (b) NCS6, (c) NCS8, and (d) NCS10 samples, respectively.

3.7 Electrochemical Analysis

To comprehend the energy storage performance of all prepared samples in 3 M KOH electrolytes, electrochemical investigations were performed in a three-electrode system (half-cell configuration) that contains reference electrode (Ag/AgCl) and a counter electrode (platinum wire) submerged in an electrolyte. The NCS samples in the slurry form were drop-casted onto Ni foam (1 cm × 1 cm) to prepare the working electrodes. The NCS ink was prepared by mixing NiCo₂S₄ sample powder, super p carbon black, and polyvinylidene fluoride (PVDF) in 80:10:10 ratio in N-methyl 2-pyrrolidone (NMP). For all the electrochemical tests, the mass loading of the as-synthesized sample was >2 mg/cm² after drying the NCS located Ni-foam at 70 °C for 6 h.

3.7.1 Cyclic voltammetry

The electrochemical performance of NCS samples as supercapacitor electrodes were examined at various scan rates of 5, 10, 15, 20, 25, 30, 40, 50, and 100 mV. The identical form of the CV curves indicates typical pseudo-battery behavior. The two redox peaks seen in the CV curves indicate the amendable diffusion of OH⁻ ions from the KOH electrolyte, which are caused by the faradaic redox reactions following the electrochemical reaction,

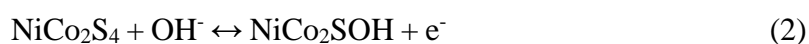


Fig. 3.8 demonstrates that the area of the curves continues to grow with the increase in the scan rate as predicted by the Randles-Sevcik equations. The symmetric and reversible shape of the CV curves suggests rapid charge transfer during the faradaic reaction mechanism at the electrode and electrolyte interface. The oxidation and reduction peaks are perceptible irrespective of scan rates. Additionally, the entry and outflow of OH⁻ ions cause the cathodic/anodic peak location to change significantly at higher and lower potentials, and an increase in scan rates indicates slower kinetics, which can be ascribed to internal resistance and charge transfer limitations.

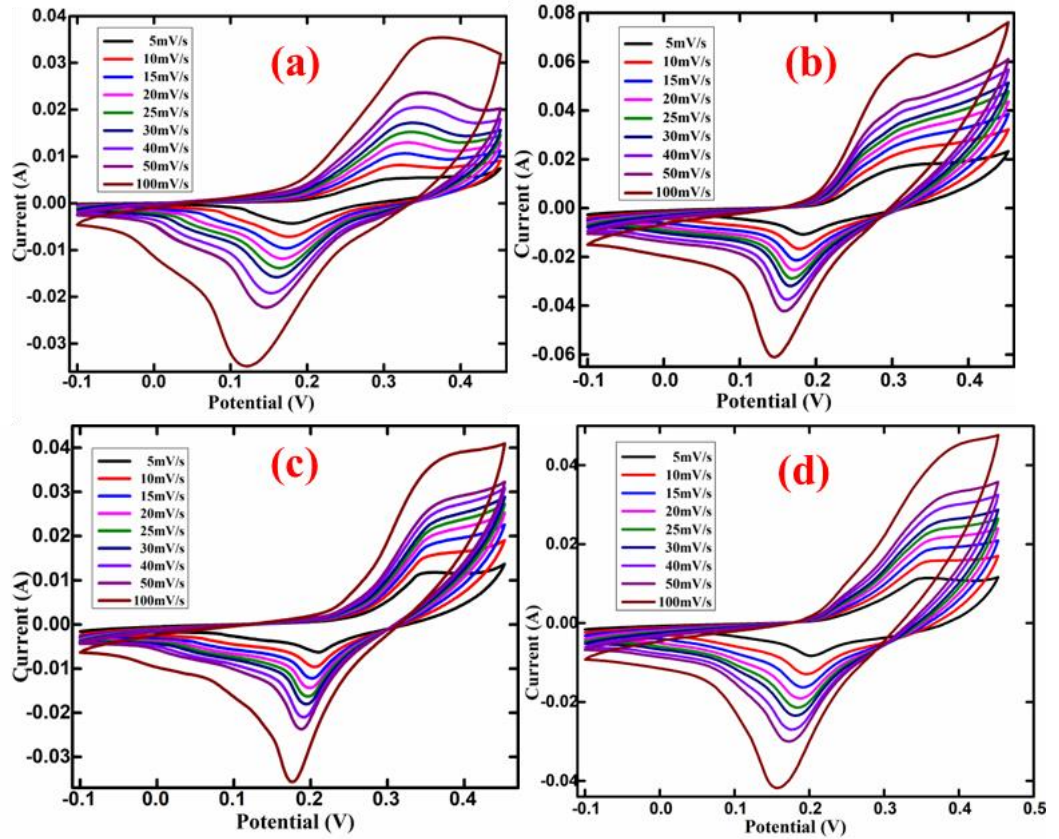


Fig. 3.8. CV curves of (a) NCS4, (b) NCS6, (c) NCS8, and (d) NCS10 samples at various scan rates.

Peak current (i_p) can be represented as total currents arising from the surface-contributed redox reactions (K_1v) and the slow semi-infinite diffusion-controlled contribution process ($K_2v^{1/2}$) under certain potential sweep rates. As stated below [37], an empirical relationship is provided,

$$i_p = av^b = K_1v + K_2 v^{1/2} \quad (3)$$

$$\text{or } \log i_p(v) = \log a + b \log(v) \quad (4)$$

Where, a and b are constants, v is the scan rate, and i_p is the current density. The current-controlled capacitive and semi-infinite diffusion-limited processes are identified as b is 1 or 0.5, respectively. In the present case, the estimated value of b is 0.696 for the NCS4, 0.635 for the NCS6, 0.572 for the NCS8, and 0.536 for the NCS10 (Fig. 3.9), representing the semi-infinite diffusion-limited process, along with the transition region that combines capacitive and battery properties.

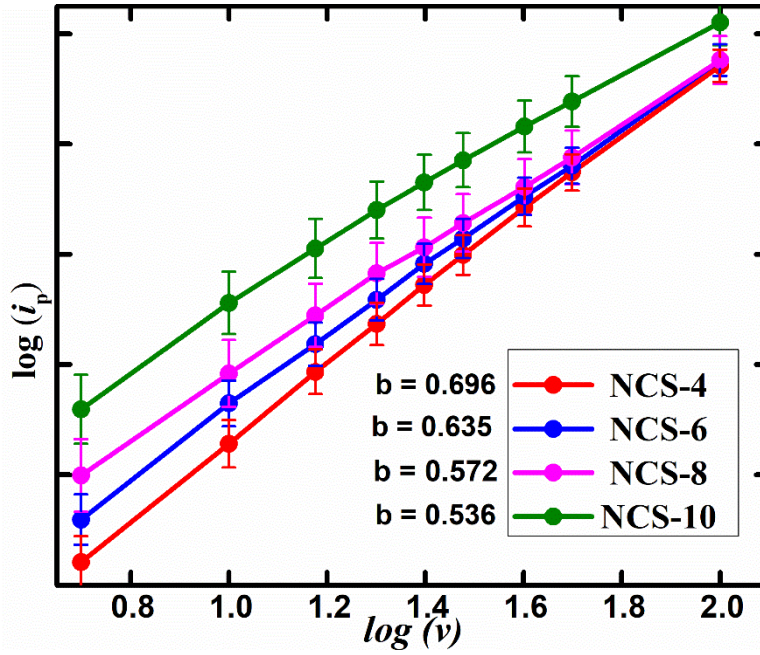


Fig. 3.9. The peak current density (i_p) of the cathodic peak current of different (a) NCS4, (b) NCS6, (c) NCS8, and (d) NCS10 samples.

Furthermore, the specific capacitance is evaluated from the CV graph using the equation,

$$C_s = \frac{\int i \, dv}{m v \Delta V} \quad (5)$$

Where, C_s = specific capacitance (F/g),

m = mass of active electrode materials (g),

v = scan rate (mV/s),

ΔV = potential range (V),

$\int idv$ = integral area of the CV curve.

The C_s value evaluated at scan rate of 5 mV/s for as-synthesized NCS samples NCS4, NCS6, NCS8 and NCS10 samples was F/g, 554.763 F/g, 419.92 F/g, 768.87, and 810.61 F/g, which decreased to 107.663 F/g, 85 F/g, 112 F/g and 157.609 F/g, respectively, at a higher scan rate of 100 mV/s. At a higher scan rate, the OH^- ions could not get sufficient time to intercalation and deintercalation over the accessible surface of nanostructures, and hence specific capacitance was reduced than that of a slower scan rate. Moreover, the NCS10 sample offering microflowers morphologies consisting of nanoflakes provided a relatively larger surface

area and hence delivered higher specific capacitance than the NCS4, NCS6, and NCS8 samples.

3.7.2 Galvanostatic charge-discharge

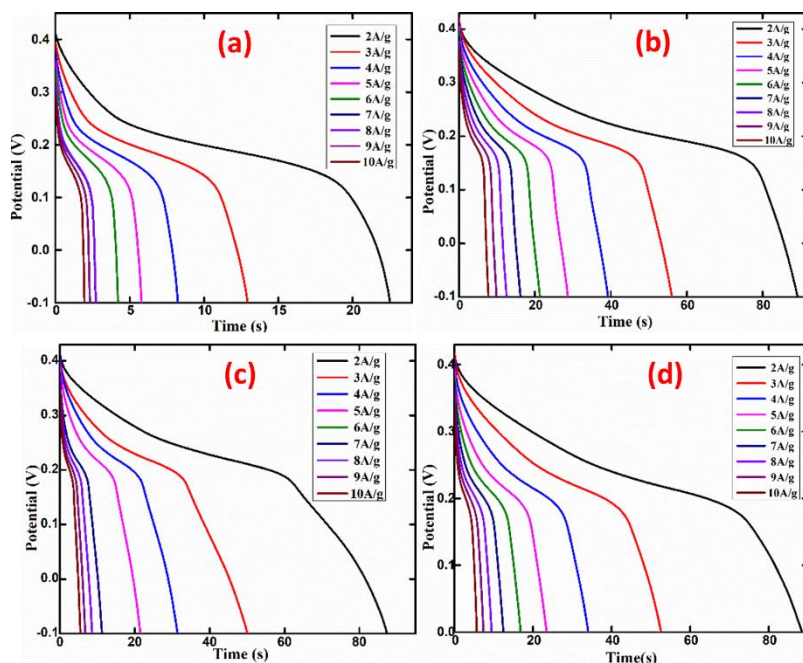


Fig. 3.10. GCD curve of (a) NCS4, (b) NCS6, (c) NCS8, and (d) NCS10 samples recorded at various current densities in the range of 2 to 10A/g. The 2.1, 2.7, 2, and 2 mg mass was loaded to prepare the electrode of NCS4, NCS6, NCS8, and NCS10 samples, respectively.

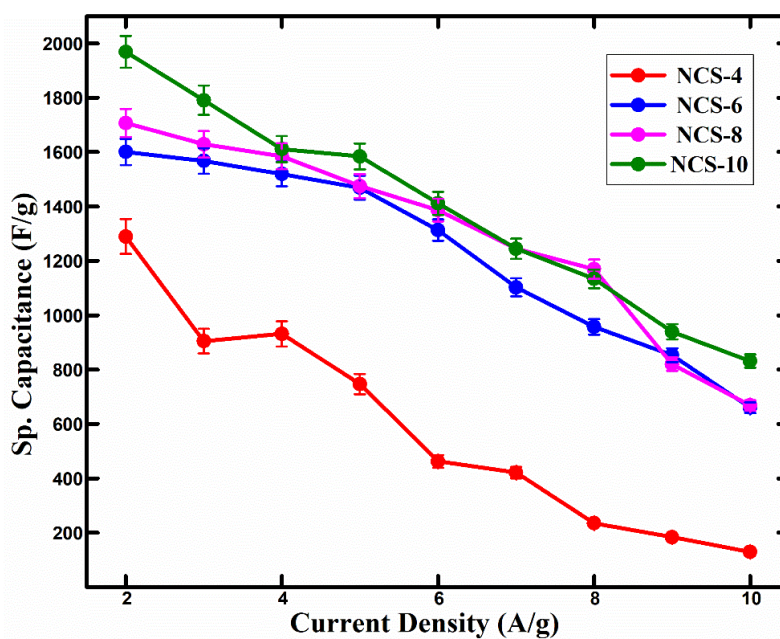


Fig. 3.11 The specific capacitance of (a) NCS4, (b) NCS6, (c) NCS8, and (d) NCS10 samples. nanostructure morphologies at various current densities.

GCD curves for as-synthesized samples, measured at different current densities in the specified potential window, are shown in Fig. 3.8. The current density and the charge-discharge time were inversely proportional. The C_s values were calculated from the GCD curves using the following equation [33],

$$C_s = \frac{I dt}{m dv} \quad (6)$$

Where, m = mass of loading (g), I = applied current (A), C_s = specific capacitance (F/g), and dt/dv = slope of the discharge curve in the GCD. The specific capacitance of 1289.512 F/g, 1643.237 F/g, 1861.820 F/g and 1968.870F/g was gained at current density of 2 A/g for the NCS4, NCS6, NCS8 and NCS10 samples, which reduced to 560.439 F/g, 600.09 F/g, 668.09, and 831.48 F/g at the current density of 10 A/g as shown in (Fig.3.11). The maximum specific capacitance of 1968.870F/g was observed at 2 A/g current density for the NCS10 sample having microflowers consisting of nanoflakes, which might be due to larger surfaces being easily accessible for the diffusion of ion deep inside the microflowers morphology compared to that of other observed morphologies.

3.7.3 Electrochemical Impedance Spectroscopy (EIS)

Along with the number of active materials and electrolytes, the electrical characteristics, material core, and textural boundaries are crucial for the effectiveness of energy storage. The effect of materials and electrolyte resistance and the shape of NCS nanostructure on the ion diffusion is determined from Electrochemical Impedance Spectroscopic (EIS). Fig.3.12 displays the Nyquist plots of representative NCS10 samples showing higher specific capacitance in 3M KOH measured over the frequency range of 0.1 Hz to 100 kHz. The equivalent circuit diagram is shown in the inset. Semicircles at a higher frequency and slightly curved lines at a lower frequency are observed. The series resistance (R_s) of 0.820 Ω and charge transfer resistance (R_{ct}) of 3.879 Ω represents the ease of ion transport along the surface of the nanoflakes.

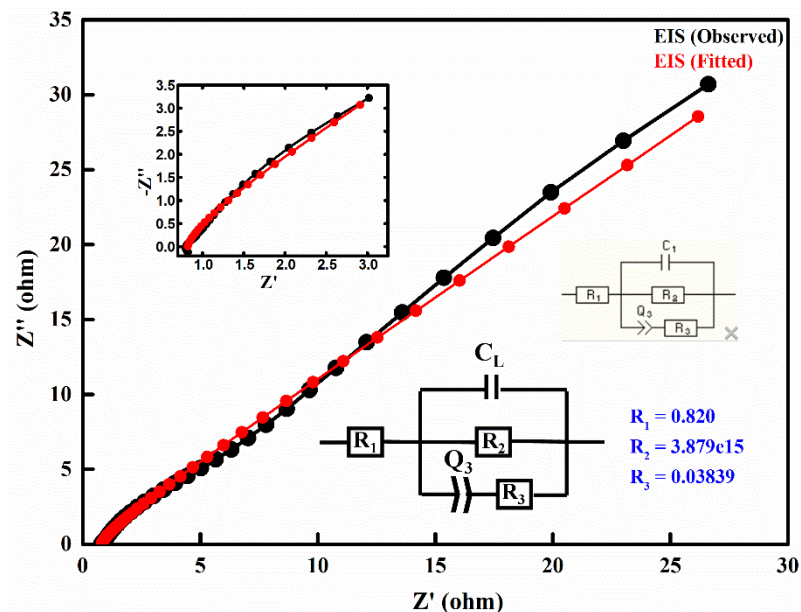


Fig. 3.12. Electrochemical Impedance Spectra of NCS10 electrode. Inset shows the equivalent circuit diagram observed for fitted data.

3.7.4 Cyclic stability

The durability of supercapacitors depends on the cyclic stability. As a result, GCD cycle performance was evaluated at a current density of 10 A/g (Fig. 3.13). After almost 5000 cycles, the specific capacitance of the NCS10 sample has a capacitance retention of 88.86% of its initial value. This demonstrates that the NCS10 sample is excellent electrode material for stable supercapacitive performance.

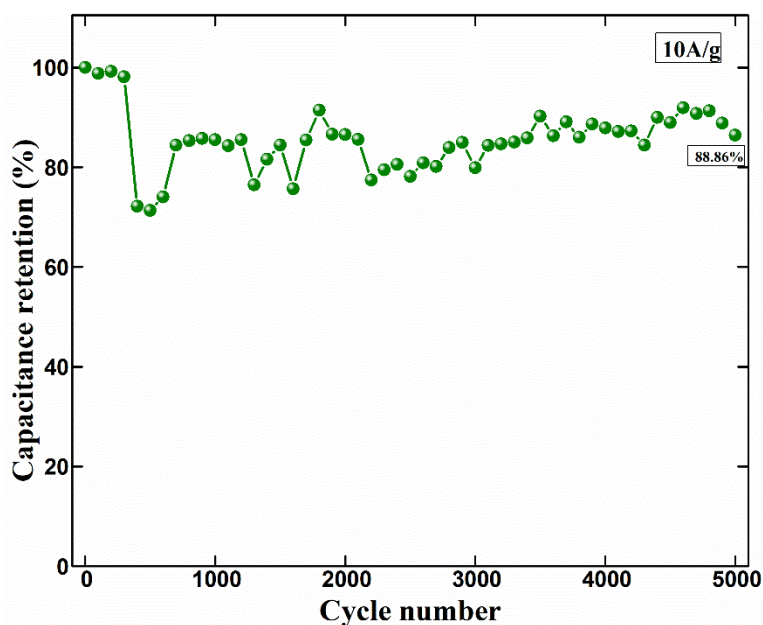


Fig. 3.13. Cycling stability studies of NCS10 electrode for 5000 continuous GCD cycles.

3.7.5 Ragone plot

A comparison of the energy and power densities of the samples is made using the Ragone plot (Fig. 3.14). The figure displays the Ragone plot for the power and energy densities calculated using equations [45].

$$E \text{ (Wh/Kg)} = \frac{1}{2} * C_s * (\Delta V)^2 / 3.6 \quad (7)$$

$$P \text{ (W/Kg)} = (E/\Delta t) * 3600 \quad (8)$$

The maximum power and energy density of 2750 W/kg and 14.254 Wh/Kg are observed for NCS10 samples, respectively.

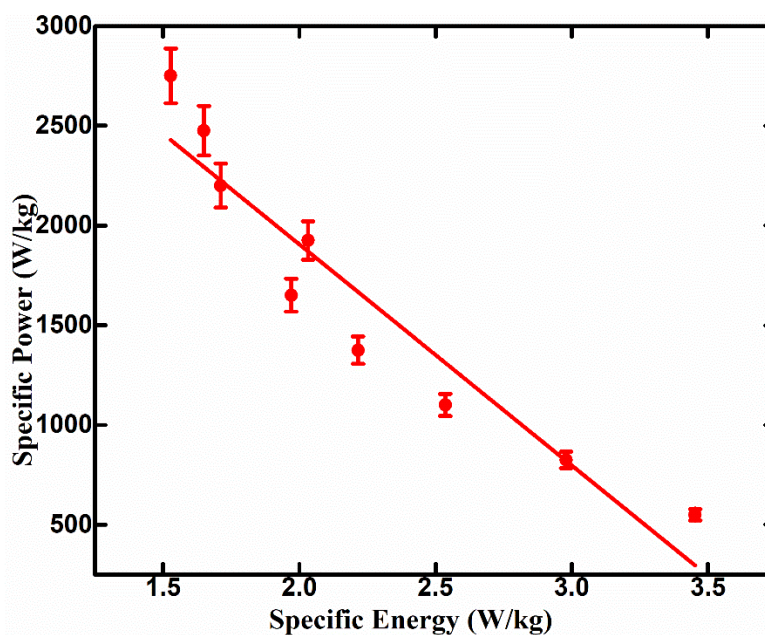


Fig.3.14 Ragone plot of the supercapacitor electrode prepared using NCS10 sample.

CHAPTER 4

Conclusion and Future Scope

Conclusion

We have successfully synthesized Nickel Cobalt Sulfide nanostructures through the hydrothermal method. Surface morphologies of the synthesized nanostructures were studied using FESEM image. Transformation of nanoparticles into spherical rose-like microflowers of 2D nano-flakes was observed with increased time. The existence of Ni, Co, S, and oxygen was confirmed by EDS spectra. XPS analysis represents the formation of pure stoichiometric NiCo_2S_4 compounds. The crystallinity of NiCo_2S_4 was confirmed, and the crystal structure was found to be cubic. The surface properties, like pore size or volume and specific surface area, were analyzed from N_2 adsorption and desorption isotherm by BET, and the specific surface area was found to be $36.671 \text{ m}^2/\text{g}$ for NCS4, $37.057 \text{ m}^2/\text{g}$ for NCS6, $33.412 \text{ m}^2/\text{g}$ for NCS8, and $28.163 \text{ m}^2/\text{g}$ for the NCS10, respectively. The thermogravimetric analysis (TGA) was performed to examine the corresponding reactions and thermal analysis of NiCo_2S_4 . The three-electrode system was employed to perform electrochemical measurements to study the redox kinetics of the synthesized NCS. The identical form of the CV curves indicates typical pseudo-battery behavior. Galvanostatic charge-discharge (GCD) was employed to calculate the electrode's specific capacitance. The specific capacitance of NCS4, NCS6, NCS8 and NCS10 samples was found to be 1289.512 F/g , 1643.237 F/g , 1861.820 F/g , and 1968.870 F/g respectively at 2 A/g which reduced to 560.439 F/g , 600.09 F/g , 668.09 , and 831.48 F/g at 10 A/g . It also showed excellent cyclic stability even after 5000 cycles at 10 A/g and retained at 88.86% of its initial C_s . EIS was done to study the electrode

processes and showed low charge transfer and diffusion resistance. The maximum power and energy density of 2750 W/kg and 14.254 Wh/Kg are observed for the NCS10 sample, respectively. Hence, we can conclude that Nickel Cobalt Sulfide (NiCo_2S_4) is an emerging material for high-performance supercapacitor electrodes.

Future Scope

- NCS electrodes will be subjected to two electrode solid state/flexible supercapacitor device fabrication for real-time application.
- Due to the synergistic effects, composites of NCS with carbon-based materials, transition metal sulfides, conducting polymers, and other 2D materials like MXene can be used to boost the electrochemical performance of the device.
- Further, the possibility of binder-free electrodes and the application of organic electrolytes and ionic liquids can be explored to get a wider potential window and higher energy density.

References

1. Jalal et al., “A review on Supercapacitors: types and components”, *Journal of Physics: Conference Series*, 1979(2021)
2. Arnia Forouzandeh et al, “Electrode Materials for Supercapacitors: A Review of Recent Advances,” *catalysts*, 10(9) 2020), 969
3. Qi Li et al, “Progress in electrolytes for rechargeable Li-based batteries and beyond,” *Green Energy & Environment*, 1(2016) 18-42
4. Narendra Kurra et al, “18 - Supercapacitor”, *Storing Energy (Second Edition)*, (2022) Pages 383-417
5. E. Goikolea et al, “Emerging Nanotechnologies in Rechargeable Energy Storage Systems”, 2017 Copyright © 2017 Elsevier Inc. All rights reserved.
6. Soubantika Palchoudhury et al, “Transition metal chalcogenides for next-generation energy storage”, *Nano advance*, 5(10) (2023) 2724–2742.
7. Rasmita Barik et al, “Challenges and prospects of metal sulfide materials Q8 for supercapacitors”, *Science Direct*, 560(2020) 1-8
8. Narasimharao Kitchamsetti et al, “Theory abide experimental investigations on morphology driven enhancement of electrochemical energy storage performance for manganese titanate perovskites electrodes”, *Journal of Power Sources*, 538 (2022) 231525
9. Anguo Xiao et al, “Hydrothermal synthesis of mesoporous metal oxide arrays with enhanced properties for electrochemical energy storage”, *Materials Research Bulletin*, 61 (2015) 54-57
10. Ting-Feng Yi et al, “NiCo₂S₄-based nanocomposites for energy storage in supercapacitors and batteries”, *Nano Today*, 33(2020) 100894
11. Jing Ye et al., “NiCo₂S₄ nanoparticles on carbon cloth with high mass loading as multifunctional electrode for hybrid supercapacitor and overall water splitting”, *Applied Surface Science*, 554 (2021) 149598.
12. Yao Li et al., “A NiCo₂S₄ /hierarchical porous carbon for high performance asymmetrical supercapacitor”, *Journal of Power Sources*, 427 (2019) 012015

13. Wenling Wu et al., “Hierarchical structure of Self-Supported NiCo₂S₄ Nanoflowers@NiCo₂S₄ nanosheets as high rate-capability and cycling-stability electrodes for advanced supercapacitor”, *Applied Surface Science*, 563 (2021)
14. Weijun Peng et al., “Synthesis of NiCo₂S₄ nanospheres/reduced graphene oxide composite as electrode material for supercapacitor”, *Current Applied Physics*, 20 (2020)
15. Xiaoyuan Liang et al., “In-situ growth of bimetallic sulfide NiCo₂S₄ nanowire on carbon cloth for asymmetric flexible supercapacitors”, *Journal of Energy Storage*, 42 (2021)
16. Long Liu et al., “NiCo₂S₄ nanosheets network supported on Ni foam as an electrode for hybrid supercapacitors”, *Journal of Alloys and Compounds*, 766 (2018)
17. Zhongchun Li et al., “Nickel cobalt sulfide nanosheets uniformly anchored on porous graphitic carbon nitride for supercapacitors with high cycling performance”, *Electrochimica Acta*, 231 (2017)
18. Le Luo et al., “NiCo₂S₄/Ni₂Co layered double hydroxide nanocomposite prepared by a vapor-phase hydrothermal method for electrochemical capacitor application”, *Journal of Alloys and Compounds*, 705 (2017)
19. Ziqian Ma et al., “Nanoporous electrospun NiCo₂S₄ embedded in carbon fiber as an excellent electrode for high-rate supercapacitors”, *Applied Surface Science*, 533 (2020)
20. Weiguo Huang et al., “Novel fabrication of hollow and spinous NiCo₂S₄ nanotubes templated by natural silk for all-solid-state asymmetric supercapacitors”, *Journal of Colloid and Interface Science*, 549 (2019)
21. Jing Li et al., “Polypyrrole-wrapped NiCo₂S₄ nanoneedles as an electrode material for supercapacitor applications”, *Ceramics International*, 47 (2021)
22. Yuting Luan et al., “Rational design of NiCo₂S₄ nanoparticles @ N-doped CNT for hybrid supercapacitor”, *Applied Surface Science*, 447 (2018)

23. Fangping Wang et al., “One-step hydrothermal synthesis of sandwich-type NiCo₂S₄@reduced graphene oxide composite as active electrode material for supercapacitors”, *Applied Surface Science*, 425(2017)
24. Xunhui Xiong et al., “Controlled synthesis of NiCo₂S₄ nanostructured arrays on carbon fiber paper for High-performance pseudocapacitors”, *Nano Energy*, 16(2015)
25. Rui Xu et al., “A Two-Step Hydrothermal Synthesis Approach to Synthesize NiCo₂S₄/NiS Hollow Nanospheres for High-Performance Asymmetric Supercapacitors”, *Applied Surface Science*, 422(2017)
26. J. Epp, “Materials Characterization Using Nondestructive Evaluation (NDE) Methods”, Woodland publishing, 2016 Elsevier Ltd. All rights reserved, Pages 17-43.
27. B.J. Inkson et al., “2 - Scanning electron microscopy (SEM) and transmission electron microscopy (TEM) for materials characterization”, *Materials Characterization Using Nondestructive Evaluation (NDE) Methods*, Woodland publishing, Copyright © 2016 Elsevier Ltd. All rights reserved, Pages 17-43.
28. Johannes Bernardi, “Energy-dispersive X-ray spectroscopy”, *Imaging Modalities for Biological and Preclinical Research: A Compendium*, Volume 1, Copyright © IOP Publishing Ltd 2021
29. Pouran Pourhakkak et al., “Chapter 1 - Fundamentals of adsorption technology”, *Interface Science and Technology*, 33(2021) 1-70
30. Nina Hwang, Andrew R. Barron, “BET Surface Area Analysis of Nanoparticles”, Version 1.1: May 8, 2011, 0500, <http://creativecommons.org/licenses/by/3.0/>
31. “Thermogravimetric Analysis (TGA)”, <https://aurigaresearch.com/pharmaceutical-testing/thermogravimetric-analysis-tga/>
32. P.K. Gallagher “Thermal Analysis: Further Developments”, *Encyclopedia of materials: Science and Technology*(Second Edition) 2001, Pages 9141-9150

33. Information for this article was taken from Thermo Electron Corp.'s website on XPS (www.lasurface.com), Operated by the University of California for the US Department of Energy
34. Tyler S. Mathis et al., “Energy Storage Data Reporting in Perspective—Guidelines for Interpreting the Performance of Electrochemical Energy Storage Systems”, *Advance energy materials*, 9 (2019) 1902007.
35. Haisheng Chen et al, “Progress in electrical energy storage system: A critical review”, *Progress in Natural Science*, 19(2009) 291-312
36. T. Brousse et al., “To Be or Not To Be Pseudocapacitive?”, *J. Electrochem. Soc.* 2015, 162, A5185.
37. Mabbott, G. A. An Introduction to Cyclic Voltammetry *J. Chem. Educ.* **1983**, 60 (9) 697– 702 DOI: 10.1021/ed060p697.
38. Danupol Boonpakdee et al., “Exploring non-linearities of carbon-based microsupercapacitors from an equivalent circuit perspective, *J. Mater. Chem. A* 2018, 6, 7162
39. Yuting Luan, et al., “Rational design of NiCo₂S₄ nanoparticles @ N-doped CNT for hybrid supercapacitor”, *Applied Surface Science* 447(2018)165-172.
40. Xin Li et al., “Electrochemical Behavior of Single Walled Carbon Nanotube Supercapacitors under Compressive Stress”, See <https://pubs.acs.org/sharingguidelines> for options on how to legitimately share published articles.
41. D.-Y.Kim et al., “Chemical synthesis of hierarchical NiCo₂S₄ nanosheets like nanostructure on flexible foil for a high-performance supercapacitor”, *Scientific Reports* volume 7, Article number: 9764 (2017)
42. J. Yang et al., “Electrochemical performances investigation of NiS/rGO composite as electrode material for supercapacitors”, *Nano Energy*, 5 (2014), pp. 74-81

43. F. Wang et al., "One-step hydrothermal synthesis of sandwich-type NiCo₂S₄ @reduced graphene oxide composite as active electrode material for supercapacitors", *Appl. Surf. Sci.*, 425 (2017), pp. 180-187
44. Kitchamsetti Narasimharao, et al. "Theory abide experimental investigations on morphology driven enhancement of electrochemical energy storage performance for manganese titanate perovskites electrodes." *Journal of Power Sources* 538 (2022): 231525.
45. Gaire, Madhu, et al. "Nanostructured manganese oxides electrode with ultra-long lifetime for electrochemical capacitors." *RSC Advances* 10.28 (2020): 16817-16825